Chemical Engineering Journal 511 (2025) 162249

Contents lists available at ScienceDirect

Chemical Engineering Journal

journal homepage: www.elsevier.com/locate/cej

Nanodiamond decorated phosphor-silicone thermally conductive PA6 composites with excellent flame retardancy, nanomechanical and thermo-pyroelectric response

Benjamin Tawiah [a,d], Sana Ullah [b], Ivan Miguel De Cachinho Cordeiro [e], Anthony C.Y. Yuen [c], Yang Ming [a], Mohammad Z. Rahman [a], Daming Chen [a], Wei Cai [a], Zheng Guangping [b], Bekeshev Amirbek [f], Lyazzat Tastanova [g], Bin Fei [a,*]

[a] School of Fashion and Textiles (SFT), The Hong Kong Polytechnic University, Hung Hom, Hong Kong SAR, China
[b] Department of Mechanical Engineering, The Hong Kong Polytechnic University, Hung Hom, Hong Kong SAR, China
[c] Department of Building, Environment and Energy Engineering, The Hong Kong Polytechnic University, Hung Hom, Hong Kong SAR, China
[d] Department of Industrial Art (Textiles), Kwame Nkrumah University of Science and Technology, PMB, Kumasi, Ghana
[e] School of Mechanical and Manufacturing Engineering, University of New South Wales, Sydney, NSW 2052, Australia
[f] Laboratory of Polymer Composites, K. Zhubanov Aktobe Regional State University, Aliya Moldagulova Avenue 34, Aktobe 030000, Kazakhstan
[g] Department of Oil and Gas, K. Zhubanov Aktobe Regional State University, Aliya Moldagulova Avenue 34, Aktobe 030000, Kazakhstan

ARTICLE INFO

Keywords:
Nanodiamonds
Surface modification
Flame retardants
Ferroelectric composites
Nanoindentation hardness
Molecular dynamic simulation

ABSTRACT

Polyamide 6 (PA6) is a widely used engineering polymer, valued for its mechanical strength and ease of processability. However, its inherent flammability, low thermal conductivity, and weak ferroelectric response restrict its applicability in advanced composite materials. In this study, a multifunctional PA6 composite was developed using phosphor-silicone decorated nanodiamonds (NDSiP), resulting in enhanced fire safety, improved thermal conductivity, superior pyroelectric response, and strengthened nanomechanical properties. The composite demonstrated a 40.7 % reduction in peak heat release rate (PHRR) and a 160 % increase in the flame retardancy index (FRI), achieving a V-0 rating and a limiting oxygen index (LOI) of 31.2 %. MD-ReaxFF simulations confirmed that the flame-retardant mechanism primarily occurred in the condensed phase, evidenced by a significant C–C peak shift towards 1.42 Å and 1.16 Å, corresponding to graphitic structure bond distances, induced by the presence of ND and oxidized phosphor-siloxane carbonaceous clusters. The thermal conductivity of the composites increased by 302 %, accompanied by substantial improvements in remnant polarization (0.208752 μC/cm2), switching polarization (0.72 μC/cm2), average permittivity (66.0), capacitance (19.5 pF), and resistivity (1.37 GΩ). Additionally, a notable enhancement in the pyroelectric coefficient ($-\partial P/\partial T$) was observed, attributed to the enhanced phase transition behavior of NDSiP within the PA6 matrix. Moreover, the composites exhibited exceptional heat dissipation capabilities, driven by the phonon heat transport effect of ND, making them suitable for thermal management applications. Significant improvements in nanoindentation hardness and Young's modulus were achieved, alongside a 123 % increase in tensile strength, highlighting the strong interfacial bonding between PA6 and NDSiP.

1. Introduction

The increasing demand for high-performance materials in industrial applications has driven the development of advanced polymer composites [1,2] that exhibit superior mechanical properties, enhanced thermal conductivity, high thermal stability, and excellent flame-retardant (FR) characteristics [3]. These attributes are particularly critical for electronic, automotive, and aerospace applications where fire safety, energy efficiency, and effective thermal management are paramount [4]. Among thermoplastics, polyamide 6 (PA6) is widely recognized for its excellent mechanical strength, chemical resistance, and moderate thermal stability [5]. However, its inherent flammability, low thermal conductivity, and limited understanding of its nanomechanical and ferroelectric properties restrict its broader application in high-

* Corresponding author.
E-mail address: bin.fei@polyu.edu.hk (B. Fei).

https://doi.org/10.1016/j.cej.2025.162249
Received 15 February 2025; Received in revised form 26 March 2025; Accepted 31 March 2025
Available online 2 April 2025

performance engineering sectors [5,6]. Addressing these limitations necessitates the development of multifunctional polymer composites capable of withstanding extreme conditions while maintaining device integrity and efficiency.

Over the past decade, extensive research has focused on fabricating multifunctional polymer composites by incorporating various fillers [7–9]. Conventional reinforcements and flame-retardant additives can enhance fire resistance but often compromise the mechanical strength and thermal stability of polymer matrices [10,11]. Recent advancements in nanotechnology have introduced new pathways for improving the multifunctionality and overall performance of polymer composites [12,13]. Among these nanomaterials, nanodiamonds (NDs) exhibit exceptional properties such as high mechanical strength, chemical inertness, thermal stability, inherent electrical conductivity, and biocompatibility, making them promising candidates for various applications, including biomedical, electronic, and structural composites [14,15].

Despite their remarkable properties, NDs tend to aggregate due to high surface energy, strong van der Waals forces, potential chemical functionalization, solvent interactions, and their physical characteristics such as shape and size [16]. To mitigate these challenges, various surface modification techniques have been employed to improve ND compatibility with polymer matrices, including chemical functionalization, physical modification, and polymer grafting [17–20]. For example, phosphorylated NDs have been successfully incorporated into polyimide and ethylene vinyl acetate matrices, resulting in improved thermo-oxidative stability and flame retardancy [21]. Similarly, hydroxyl-rich ND/poly(vinyl alcohol) composites have demonstrated superior interfacial adhesion and enhanced thermal conductivity compared to their pristine counterparts [22]. Surface modifications not only facilitate ND dispersion but also optimize their performance within polymer matrices, making them ideal candidates for advanced multifunctional composite fabrication [23,24]. Given their high thermal conductivity, wide bandgap (~5.5 eV), and high electron mobility, NDs are particularly advantageous for the development of next-generation high-performance materials [25,26].

Multifunctional thermoplastic composites with pyroelectric properties offer exciting opportunities for energy applications and sensor technologies [27]. Pyroelectric materials generate an electrical charge in response to temperature fluctuations, making them valuable for energy harvesting and waste heat conversion [27,28]. This capability is particularly significant for sustainable energy solutions, enabling devices to harness ambient heat and convert it into usable electricity. Traditionally, pyroelectric materials have been ceramic-based, which limits their flexibility and application in flexible electronics [29]. The integration of carbon-based nanomaterials into polymer matrices represents a breakthrough in multifunctional composite design by offering lightweight, cost-effective, and highly customizable alternatives suitable for energy harvesting, wearable electronics, and biomedical applications [30,31]. The enhanced toughness of polymer-based composites further broadens their applicability in advanced engineering fields [13,32].

A thorough understanding of the nanoindentation microhardness of such composites provides critical insights into their mechanical performance [33,34]. The interplay between thermal conductivity, mechanical strength, flame retardancy, and pyroelectric response is crucial for optimizing composite formulations. Although significant advancements have been made in the development of multifunctional polymer composites [35–37], achieving an optimal balance between these properties remains challenging. Current studies highlight the potential of phosphorylated and hydroxylated NDs in enhancing thermal conductivity and flame retardancy [38]. However, the integration of ND-modified phosphor-silicone into PA6 to optimize thermal conductivity, nanomechanical performance, and pyroelectric response for potential energy applications remains relatively underexplored.

This study aims to address these gaps by fabricating a multifunctional composite using ND-decorated phosphor-silicone in a thermoplastic PA6 matrix to enhance thermal conductivity, flame retardancy, and nanomechanical performance while improving pyroelectric response. Additionally, we investigate the fundamental interaction mechanisms within ND-polymer composites using Reactive Molecular Dynamics (MD-ReaxFF) simulations to elucidate the charring mechanisms of modified NDs within the PA6 architecture. The developed multifunctional composite effectively mitigates the limitations of conventional polymer systems by improving fire safety, thermal management, and mechanical resilience, thereby advancing the field of high-performance polymer composites for energy conversion and other critical applications.

2. Experimental

2.1. Materials

Borane-tetrahydrofuran (BH_3·THF) complex (1 M solution in THF, stabilized), hydrochloric acid, 3-aminopropyltriethoxysilane (APTES), super dry tetrahydrofuran (THF), triethylamine (TEA), and chlorodiphenylphosphine (DPC) were procured from Aladdin Industrial Co., Ltd. (Shanghai, China). Diamond powder (Type: DND) was obtained from Beijing Grish Hitech Company. All chemical reagents were utilized without further purification. Deionized water was used as required throughout the experimental procedures.

2.2. Synthesis of Phosphor-Silicone decorated nanodiamond (NDSiP)

2.2.1. Synthesis of ND-OH

The thermal oxidation of nanodiamonds (NDs) was carried out following previously reported methods [39]. The synthesis route for NDSiP is schematically presented in Scheme 1. Initially, 5 g of ND powder was placed in a ceramic crucible and heated in a box furnace at a rate of 5 °C/min up to 600 °C in the presence of air, with a dwell time of 1 h. The oxidized ND powder was allowed to cool to room temperature before being removed from the furnace.

Subsequently, 40 mg of the oxidized ND powder was transferred to a round-bottom flask equipped with a magnetic stirrer bar and a condenser. To maintain an inert environment and prevent undesirable reactions with oxygen or moisture, the flask was securely sealed and connected to a Schlenk line. Nitrogen (N_2) gas was purged through the system to establish a controlled reaction atmosphere. A 5 mL aliquot of a 1 M BH_3·THF solution was then carefully introduced into the flask using a syringe. The reaction mixture was continuously stirred to ensure uniform dispersion and efficient interaction between the reactants. The solution was heated to a reflux temperature of 67 °C and maintained under these conditions for 24 h, with continuous nitrogen purging to preserve the inert environment and maximize product yield and purity.

The reaction was subsequently quenched by the careful addition of 2 M HCl, with monitoring to ensure the complete cessation of H_2 gas evolution. The modified NDs were recovered from the reaction mixture via successive centrifugation using acetone until a neutral pH (pH 7) was achieved, followed by thorough washing with deionized water.

2.2.2. Synthesis of Amino-Functionalized ND

The amino-functionalization of ND was performed according to a previously described method [36]. In brief, 1.0 g of ND-OH was dispersed in 140 mL of super dry THF under constant magnetic stirring and purged with N_2 to eliminate moisture. A 40 mL aliquot of a 5 % APTES solution in dry THF was introduced into the mixture via a syringe to minimize exposure to air. Once the APTES solution was added, the reaction mixture was stirred magnetically for 43 h to ensure complete functionalization.

Following the reaction period, the modified ND was separated by centrifugation, and the solid product was subjected to multiple washings to remove unreacted components. The final amino-functionalized ND was dried under a vacuum, yielding a light grey powder.

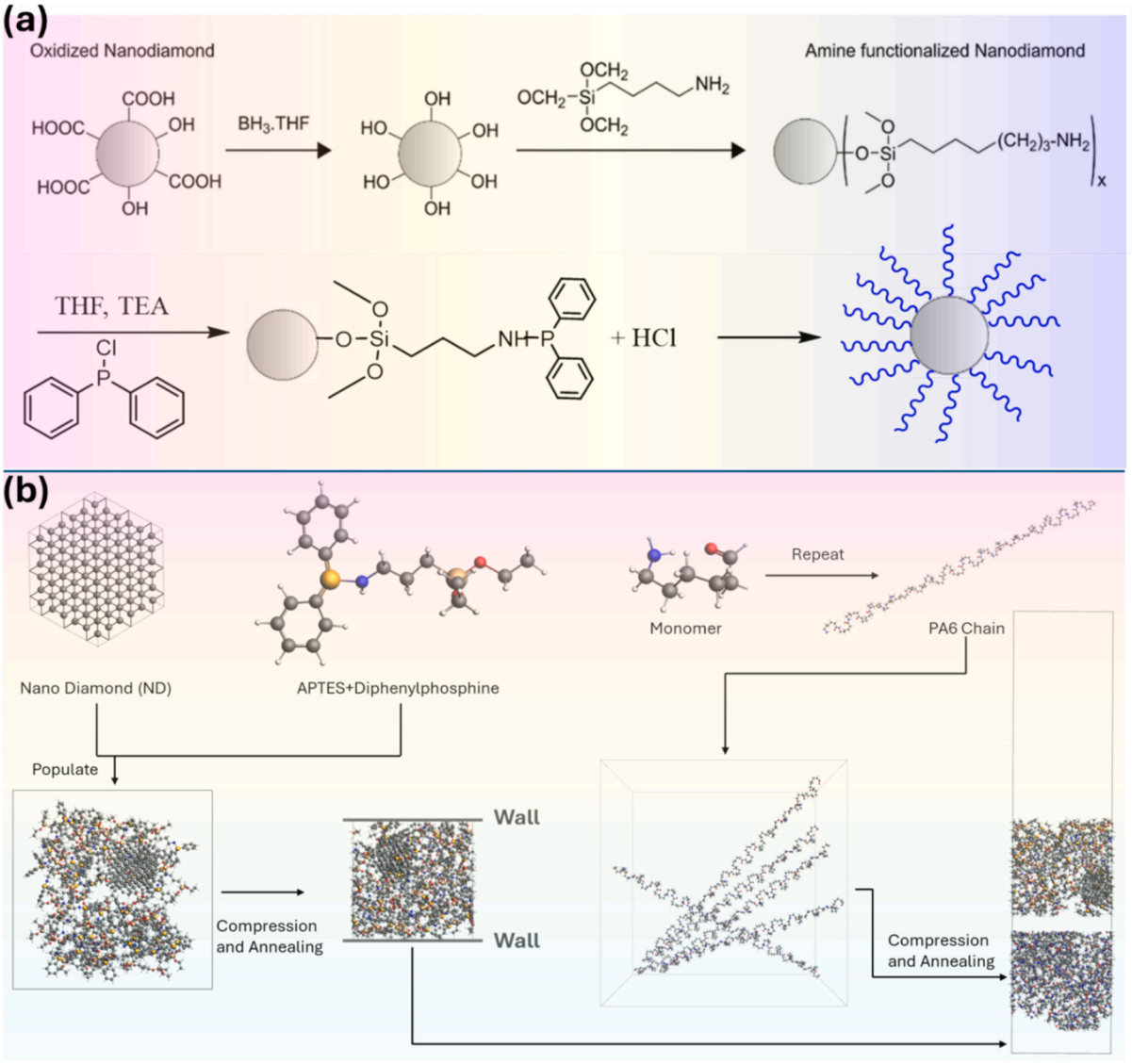

Scheme 1. (a) Synthetic procedure for NDSiP, (b) MD-ReaxFF simulation process.

2.2.3. Synthesis of Phosphorus-Functionalized ND

To achieve phosphorus functionalization, 1 g of amino-functionalized ND was dispersed in 140 mL of super dry THF in a three-necked round-bottom flask under nitrogen protection at 67 °C. Next, 2 mL of TEA was carefully added to the reaction mixture using a syringe under continuous stirring. Subsequently, 5 mL of DPC was introduced dropwise into the solution and stirred continuously for 24 h to facilitate functionalization.

After completion of the reaction, the mixture was centrifuged with acetone several times until a neutral pH (pH 7) was reached. The resulting phosphorus-functionalized ND was then dried in a vacuum oven, yielding a lighter grey powder, referred to as NDSiP.

Furthermore, Reactive Molecular Dynamics (MD-ReaxFF) simulations (Scheme 1b) were employed to investigate the interactions between NDSiP molecules and PA6 polymer chains. This approach provided crucial insights into the flame-retardant (FR) mechanism of NDSiP and its effect on the pyrolysis behavior of PA6. A detailed description of the MD-ReaxFF simulation methodology is available in the supplementary materials.

2.3. Preparation of PA6/NDSiP composites

Prior to use, PA6 granules were dried in an oven at 100 °C for 24 h. The dried granules were then blended with NDSiP using a 16 mm twin-screw extruder (Haake Rheomex PTW16, Thermo Scientific) at varying weight percentages (see Table S1). The screw speed was maintained at 30 rpm, and the temperature in the three heating zones was consistently set at 230 °C. To ensure uniform dispersion of NDSiP within the PA6 matrix, the extruded PA6/NDSiP composites were pelletized and reprocessed twice.

Subsequently, the composites were subjected to further processing using an automatic hydraulic press equipped with a mold at 240 °C. The composite samples were initially sandwiched between two hot plates and pressed at 10 bars for 4 min, followed by pressure release and degassing. The pressing process was repeated at 15 bars for an additional 1 min. To solidify the composite structure, the samples were transferred to a water-cooled section for 1 min before being removed from the mold. This process resulted in the formation of PA6/NDSiP nanocomposites. For comparison, pristine PA6 samples were prepared following the same procedure. The composite samples required for tensile testing, nano-indentation, and ferroelectric analysis were molded using appropriate templates under the same processing conditions.

2.4. Characterization

The thermal and oxidative properties of pristine NDs, modified NDs, PA6, and their composites were analyzed using a TGA/DSC 1 Star System (Mettler Toledo, Switzerland). The thermogravimetric analysis (TGA) was conducted within a temperature range of 40–600 °C at a heating rate of 20 °C/min using samples weighing between 3 and 6 mg. The percentage of weight loss was recorded as a function of temperature. The thermal conductivity of PA6 and its composites was measured at room temperature using the Netzsch laser flash thermal diffusivity technique (Netzsch, LFA 467). The thermal conductivity was calculated using Eq. (1):

$$K = \alpha x \rho x \mathbb{C}\rho \quad (1)$$

where α represents the thermal diffusivity (m2/s), ρ is the density (g/cm^3), and C_p is the specific heat capacity (J/(g·K)). The chemical composition of modified ND and the char residues after combustion were analyzed using a Perkin Elmer FT-IR spectrometer with an attenuated total reflectance (ATR) accessory. Spectra were recorded over the 4000–650 cm^{-1} range at a resolution of 4 cm^{-1}, averaging 16 scans at room temperature. The structural characteristics of char residues were further examined using a Raman Microscope (Bay Spec 3-in-1 Nomadic Raman), employing a 532 nm laser light source over the 4000–300 cm^{-1} range at room temperature. For limiting oxygen index (LOI) tests, five samples of each composite formulation were prepared. The PA6/metallic phosphide composites (dimensions: 130 × 6.5 × 3 mm) were tested according to ASTM D2863-97 using the ZR-1 Intelligent Oxygen Index Analyzer (China). The UL-94 vertical flame test was conducted in a vertical flame chamber in accordance with ASTM D3801, using five specimens per composition (130 × 13 × 3.2 mm each). The cone calorimeter test (Fire Testing Technology Ltd., UK) followed ISO 5660-1 guidelines, using three specimens per composition (100 × 100 × 4 mm) under an irradiation heat flux of 35 kW/m^2. The surface morphology of the composite samples was examined using scanning electron microscopy (SEM) (JEOL JEM-2100F, Japan) at various magnifications. The tensile properties of PA6 and PA6/NDSiP composites were evaluated using a universal electromechanical testing machine (INSTRON 3384, MA). Five dumbbell-shaped specimens (50 × 4 × 0.29 ± 0.31 mm) were tested at room temperature in accordance with ASTM D638, with a crosshead speed of 10 mm/min. For the thermal management test, composite samples were placed on a hot plate heated to 100 °C, and an infrared camera was used to monitor and record the temperature evolution over 40 s. The polarization–electric field (P–E) hysteresis loops of the samples were obtained using a TF Analyzer 2000E (aixACCT, Aachen, Germany) at room temperature. The hysteresis amplitude ranged from 500 to 8000 kV, with a sample thickness of 50

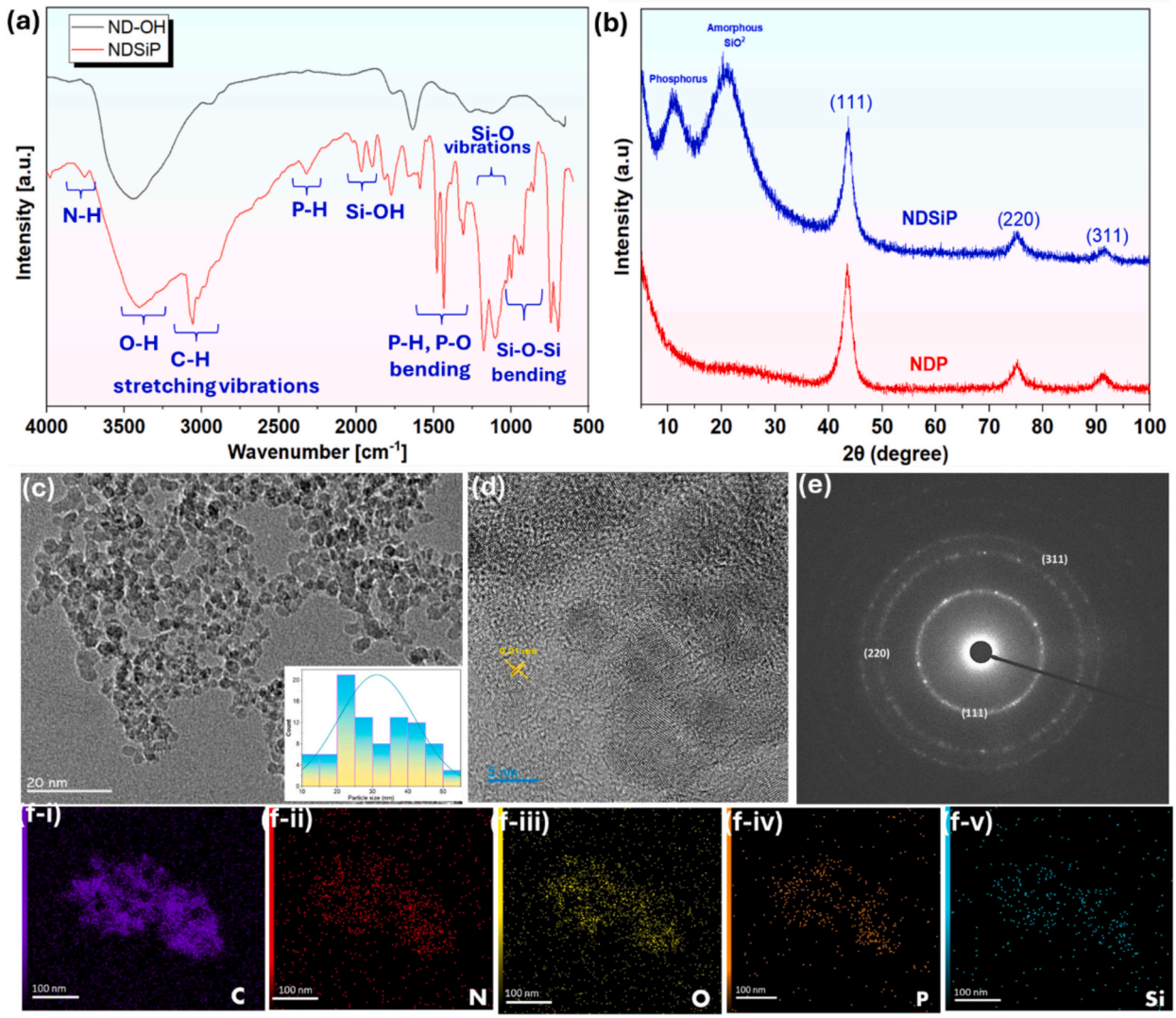

Fig. 1. Chemical and morphological properties of modified ND (a) FTIR spectra, (b) XRD crystallography, (c) TEM image of modified ND (Insert: particle size distribution), (d) approximate interlayer spacing of modified ND, (e) SAED, and (f) TEM EDS mapping of modified ND.

mm. The temperature-dependent polarization was measured between 30 and 100 °C at 10 Hz. Nanoindentation tests were conducted by securely mounting the samples on an iron base and positioning them on the magnetic stage of a HYSITRON T1970 triboindenter. Calibration of the Berkovich diamond indenter was performed using a quartz standard. Indentation areas were examined using both visible light and a scanning probe microscope attached to the triboindenter. A minimum of three indentations were made on each sample, with the average value recorded. For both PA6 and its composites, a linear load-hold-unload profile was applied, maintaining a 2-second hold period for each indentation. The modulus and hardness values were calculated by analyzing the unloading curve slope and maximum indentation depth.

3. Results and Discussion

3.1. Chemical and morphological properties of modified ND

The FTIR spectra analysis (Fig. 1a) indicates that the phosphor-silicone modification significantly altered the chemical environment of the nanodiamonds (NDs). A broad peak observed around 3200–3600 cm^{-1} in the ND-OH sample corresponds to O–H stretching vibrations, which result from BH_3 treatment, in agreement with previous findings [40]. Additionally, peaks in the range of 1300–1600 cm^{-1} correspond to C–C and C=C bonds present in the diamond structure. In the NDSiP sample, peaks associated with Si-O-Si stretching are detected around 1000–1200 cm^{-1}, confirming the presence of siloxane groups. Further, N–H vibrations are evident near 3600 cm^{-1}, along with stretching vibrations around 3200–3300 cm^{-1}. The P-O and P-H stretching and bending vibrations are observed within the 1200–1400 cm^{-1} range, along with characteristic phosphonate species vibrations near 1140 cm^{-1} (P=O stretching). Overlapping bands in the 900–1100 cm^{-1} region, arising from P-O and P-O–H groups, are also noted, aligning with previously reported findings [21]. Additionally, the diminished S-H stretching vibrations between 2550–2600 cm^{-1} suggest that thiol (−SH) groups on the nanodiamond surface were modified by the phosphorous compound. To further confirm ND modification, X-ray diffraction (XRD) analysis was performed on ND and NDSiP, as shown in Fig. 1b. Peaks corresponding to amorphous SiO_2 and phosphonate species appear at approximately 20° and 15° (2θ), respectively, consistent with literature reports [41]. The transmission electron microscopy (TEM) image (Fig. 1c) reveals that NDSiP nanoparticles exhibit an average particle size of 40.2 nm, with a narrow size distribution (see Fig. 1c insert) and an interlayer spacing of 0.21 nm, which aligns with existing literature [42]. The selected area electron diffraction (SAED) pattern in Fig. 1e further confirms the diamond crystal structure, as no distinct diffraction rings characteristic of a graphite crystal structure are observed. This finding suggests that the shell surrounding the diamond core is not composed of multi-layered graphite but rather a single-layered graphitic material, similar to the literature [42]. Additionally, the crystal structure remains unaffected by surface modification, which is consistent with previous studies [43,44]. Furthermore, the energy-dispersive X-ray spectroscopy (EDS) mapping of NDSiP (Fig. 1f, i–v) confirms the presence of carbon (C), nitrogen (N), oxygen (O), phosphorus (P), and silicon (Si), further verifying the successful modification of nanodiamonds.

3.2. Thermal properties

The thermal stability analysis of NDSiP and NDP, as shown in Fig. 2, was performed over a temperature range of 50 to 800 °C, revealing distinct thermal stability profiles. The TGA and DTG curves for NDP indicate a stable mass up to approximately 600 °C, consistent with the reported high thermal stability of ND [45]. A weight loss of

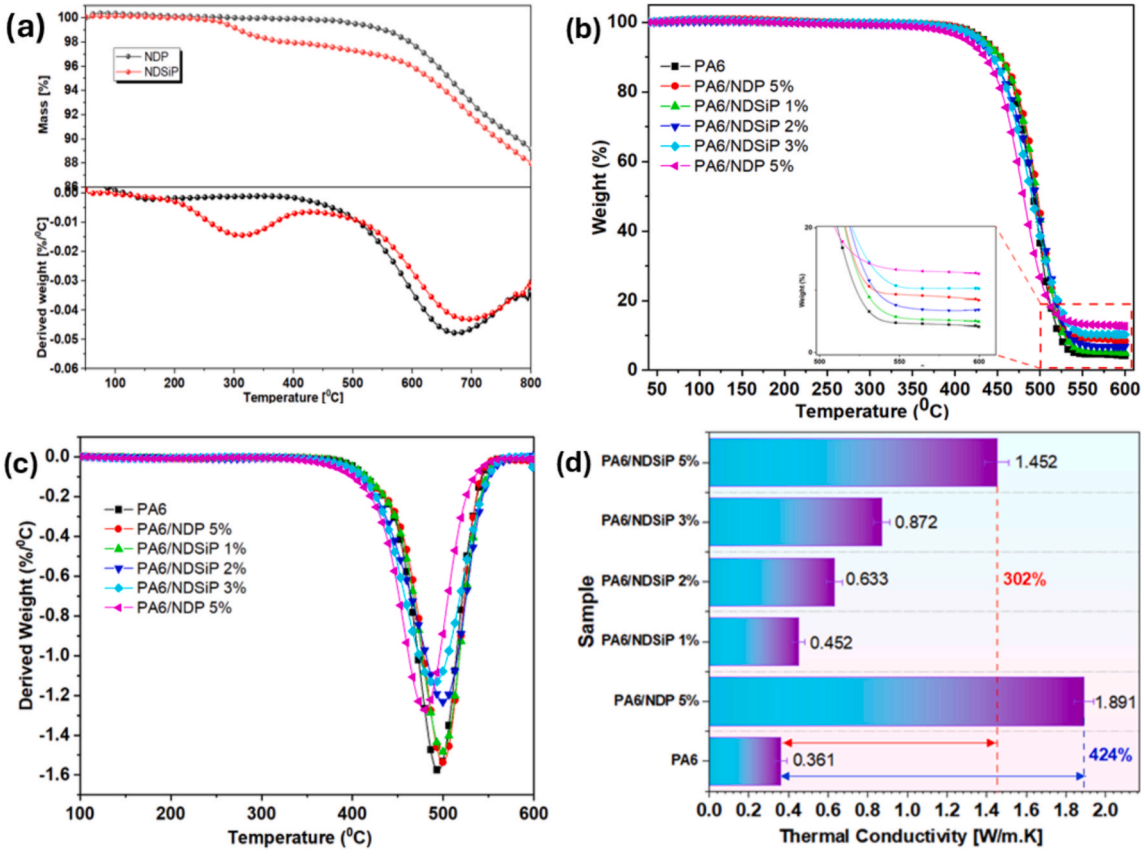

Fig. 2. Thermal stability of (a) TGA/DTG curve of oxidized and modified ND, (b) TGA curve of PA6 and PA6/ND composites, (c) DTG curve of composites, and (d) thermal conductivity of composites.

approximately 10 % was observed between 600–800 °C, attributed to the decomposition of residual organic moieties and the catalytic degradation of sp^3 carbon in ND, resulting from thermal cracking and the formation of smaller hydrocarbons [46]. Conversely, the TGA curve for NDSiP exhibits a more pronounced weight loss around 400 °C, suggesting the presence of less thermally stable functional groups introduced during the phosphor-silicone modification process. By 800 ^{0}C, the total weight loss in NDSiP reaches approximately 12 %, indicating the presence of additional volatile components or less stable organic residues on the ND surface. Additionally, the DTG curve for NDSiP shows sharp degradation peaks between 400 and 600 °C, corresponding to the rapid breakdown of phosphor-silicon groups. This degradation leads to the release of phosphorus-containing volatiles, siloxane species, and other non-combustible gases, which help suppress the thermal cracking of sp3 carbon structures. The thermal stability of NDSiP/PA6 composites is presented in Fig. 2(b–c) and Table 1. These composites exhibited a single-stage decomposition pattern, similar to that of pristine PA6, with the maximum mass loss occurring at approximately 480–500 °C. As indicated in the DTG curve and Table 1, PA6 alone had a Tmax of 493.6 °C, with a derived mass loss of −1.58 %/°C. The PA6/NDP (5 %) composite displayed the highest Tmax of 500.4 °C, albeit with a slightly lower derived mass loss of −1.53 %/°C. Upon incorporating NDSiP into PA6 at different loadings, Tmax and the derived mass loss decreased gradually, indicating early degradation of the organic functional groups (phosphorus, silicon, and nitrogen) present on the ND surface. However, as depicted in Table 1 and Fig. 2(b) (inset), this early degradation promotes the release of non-combustible gases, which in turn catalyze stable char formation. This char plays a key role in retarding composite decomposition, contributing to the material's fire resistance.

The thermal conductivity of the composites was also evaluated, with results illustrated in Fig. 2(d). The introduction of NDP (5 %) into PA6 led to an increase in thermal conductivity from 0.361 W/m·K (pristine PA6) to 1.891 W/m K, representing a 424 % improvement. This enhanced thermal conductivity of NDP is attributed to its intrinsic crystalline structure, which offers exceptional thermal conductivity, along with its strong interfacial bonding with PA6. This interaction reduces phonon scattering at the interface, facilitating the formation of efficient thermally conductive pathways. However, when NDSiP was introduced into PA6 at different loadings, the thermal conductivity increased gradually, with the PA6/NDSiP (5 %) composite exhibiting a 302 % improvement over pristine PA6. The relatively lower thermal conductivity of NDSiP compared to NDP is likely due to the presence of organic moieties (phosphorus, silicon, and nitrogen) on the ND surface. These groups can disrupt the ordered lattice structure, thereby increasing phonon scattering and limiting the effective heat transfer capability of modified ND.

3.3. Forced flame combustion behaviour

The flammability of PA6/NDSiP composites was investigated using a cone calorimeter and the results are presented in Fig. 3 and Table S2. Pristine PA6 ignited in approximately 61 s after exposure to 35 kW/m^2 heat flux with the entire combustion cycle lasting for ~700 s and generating a peak heat release rate (PHRR) of 700 kW/m^2, a total heat release (THR) of ~117 MJ/m^2, an average effective heat of combustion (AEHC) of ~16.4 MJ/kg, leaving behind a meagre char of 0.9 %. Upon the introduction of NDP, the PHRR increased marginally to ~718, however, the THR, and AEHC reduced to 114 MJ/m^2 and 14.8 MJ/kg along with a marginal increase of residual char by 3.9 %. Similarly, the average rate of heat emission (ARHE) and the average CO_2 improved by ~9.2 % and 17.6 % respectively (refer to Table S2). This phenomenon could be attributed to the catalytic behaviour of NDP in promoting faster reactions which contributed to a spike in heat release during peak degradation. However, the high thermal conductivity of NDP allows heat to travel more easily by phonon scattering, resulting in efficient heat dissipation throughout the material leading to a more controlled combustion process over time, reducing the average heat emission rate. Moreover, NDP creates a dual heat sink and dissipative effect by absorbing and redistributing heat within the composite [47], leading to a decrease in the average rate of heat emission despite an initial spike in heat release. Subsequently, upon the introduction of NDSiP at various weight fractions, the PHRR and the THR reduced significantly as shown in Fig. 3(a–b). Typically, the PA6/NDSiP 5 % resulted in a 40.7 % reduction in PHRR, a 45.3 % reduction in THR, a 28.1 % reduction in AEHC and an 18.1 % reduction in ARHE. The following improvement could be attributed to the combined effect of several factors including the phosphorus radical reaction with volatile free radicals and other combustion gases in the gas phase, which effectively inhibits combustion reactions and reduces flame intensity. As shown in Fig. 3c, NDSiP 5 % showed early mass loss attesting to the early release of non-combustible gases and radicals. At the same time, silicon can enhance this effect by promoting the formation of silicate compounds during combustion which further stabilizes the decomposition in the condensed phase as shown by the increased residual char in Fig. 3 (c insert) and Table S2. Moreover, the interaction between phosphorus and silicon during combustion along with the heat sink and dissipative properties of ND promotes stable and cohesive char formation [23] which can effectively insulate the material from heat and limit the escape of flammable gases.

Carbon monoxide (CO) is a toxic gas that is often generated from the processes of incomplete combustion. Hence, lower CO production is desirable in engineered polymeric materials fire safety as it reduces the risk of toxic gas exposure in the gas of fire accident. Fig. 3d illustrates the CO production over time for various polymer composites with the PA6 showing a comparatively low and steady CO production whereas the NDP and NDSiP PA6 composites influence CO production differently, with a notable increase in CO levels as the concentration of NDSiP increases. A distinct peak in COP can be observed around 200 s for all composites with varying intensities. The PA6/NDP composite showed the highest peak as depicted in Fig. 3(d), indicating more substantial incomplete combustion. The PA6/NDSiP composites (especially at higher concentrations) also showed relatively higher peaks, but lower than the PA6/NDP peak suggesting that NDSiP effectively reduces the intensity of combustion, potentially due to the ability of NDSiP to promote stable char formation. This stable char layer acted as a barrier, limiting the release of volatile organic compounds (VOCs) and other combustion byproducts, thus, contributing to reduced COP and total smoke production shown in Table S2. To further gain insight into the fire performance of the composites, the smoke-to-heat release ratio (SHRR) and the flame retardancy index were determined according to Eqs. (2) and (3), respectively, and the results are shown in Fig. 3(e).

$$SHRR = \frac{TSP}{THR} \tag{2}$$

where TSP is the total smoke produced by PA6 and the composites, and THR is the total heat release.

Table 1
TGA and DTG decomposition of NDP, NDSiP, and PA6 composites.

Sample	$T_{-5\%}$ (°C)	T_{-max} (°C)	Derived M.L T_{-max} (%/°C)	Residue (wt %) at T_{-max} 700 °C	
NDP	659.2	671.3	− 0.05	94.5	89.2
NDSiP	624.7	683.7	− 0.05	92.7	88.1
Pristine PA6	437.8	493.6	−1.58	47.7	3.8
PA6/NDP 5 %	436.7	500.4	− 1.53	39.1	8.3
PA6/NDSiP 1 %	435.9	498.9	−1.48	45.1	4.6
PA6/NDSiP 2 %	427.7	498.7	−1.34	43.6	6.7
PA6/NDSiP 3 %	430.8	491.3	−1.13	47.2	10.1
PA6/NDSiP 5 %	416.4	480.5	−1.28	51.1	12.9

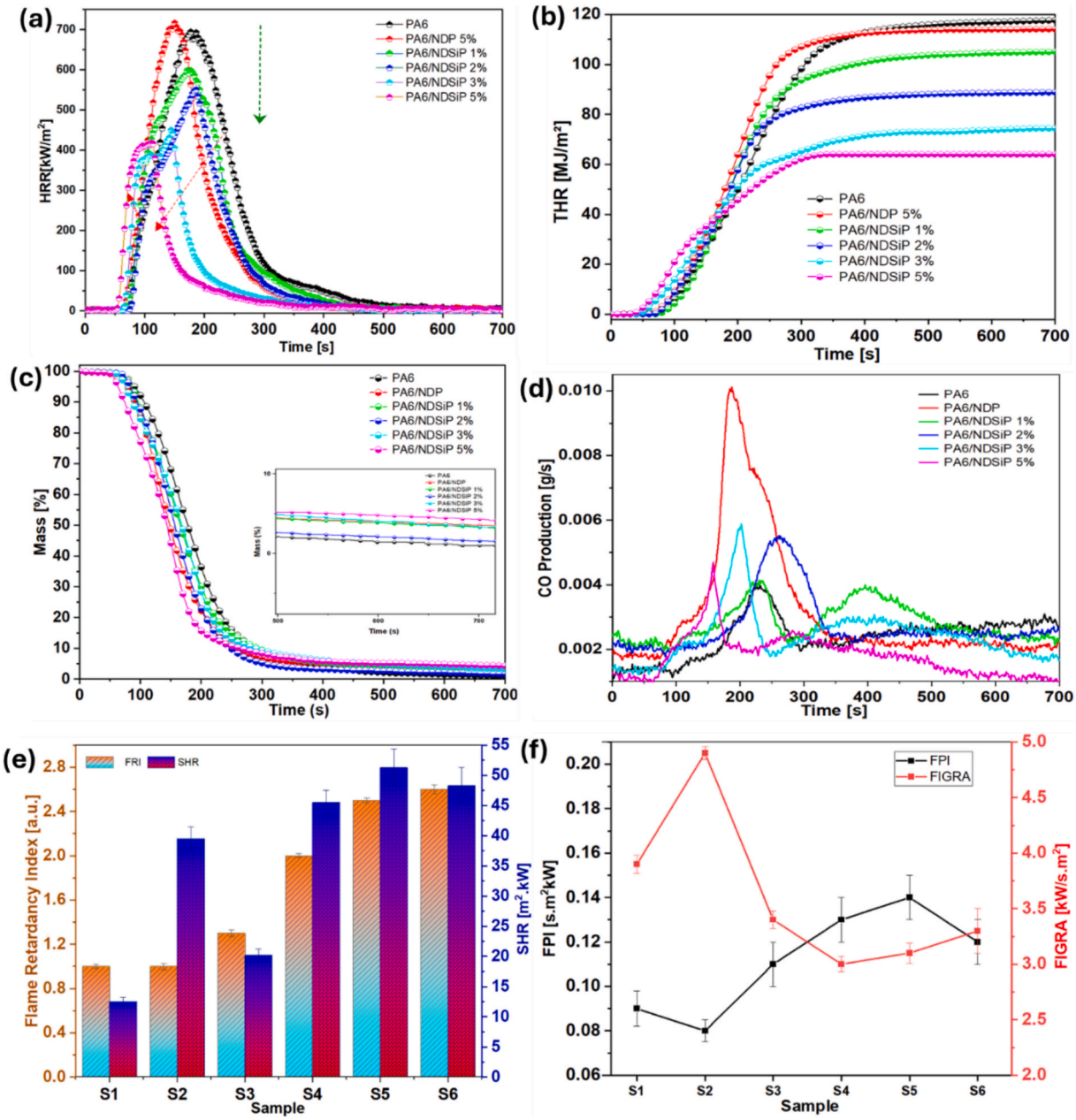

Fig. 3. Cone calorimeter results (a) Heat release rate, (b) Total heat release, (c) Mass loss, (d) carbon monoxide production, (e) Flame retardancy index and smoke to heat release, and (f) Fire performance index and fire growth rate assessment. *Note: S1- PA6, S2 – PA/NDP, S3 – PA6/NDSiP 1 %, S4 – PA6/NDSiP 2 %, S5 – PA6/NDSiP 3 %, S6 – PA6/NDSiP 5 %.*

$$FRI = \frac{\left[THR^{*}\left(\frac{PHRR}{TTI}\right)\right]_{Neatpolymer}}{\left[THR^{*}\left(\frac{PHRR}{TTI}\right)\right]_{Composite}} \quad (3)$$

Smoke-to-heat release ratio (SHRR) is a crucial composite index that provides insights into the combustion behavior and overall safety of composites in fire scenarios. Composite materials with a high SHRR are often preferred in applications where smoke toxicity and visibility are critical concerns, especially in building materials, and transportation structures. As shown in Fig. 3(e), the SHRR increased gradually as the content of NDSiP increased in PA6 with the 5 wt% NDSiP loading achieving a 286.4 % increase in SHRR indicating the potential to minimize smoke hazards during fire accidents. The feature is critical for building occupant safety during fire evacuation exercises. However, the composites produced relatively higher smoke compared to the pristine PA6 as shown in Table S2 and Fig. S1. The PA6/NDP 5 % produced relatively higher smoke due to the high thermal conductivity of ND, which allows rapid heat distribution within the PA6 matrix. This can lead to more uniform heating and quicker ignition of the material, resulting in increased combustion rate and smoke production. This is further exacerbated by the thermal cracking of the sp3 carbons in ND at high temperatures contributing to particulate matter release and smoke production instead of promoting char formation. Also, the FRI of the composite improved gradually as the content of NDSiP increased with the 5 wt% loadings achieving ~160 % relative to the pristine PA6. Similarly, the fire performance index (FPI) and the fire growth assessment (FIGRA) provide a composite index that combines various fire performance metrics for the fire safety of composite materials [48]. As shown in Fig. 3(f), the FPI decreased marginally with the 5 wt% NDP loading and subsequently improved significantly with the increasing

content of NDSiP loading; however, the performance declined marginally when the NDSiP content loading reached 5 wt%. Excessive loading of NDSiP can lead to thermal degradation at high temperatures and the release of flammable gases. This decomposition can contribute to fire propagation rather than inhibit it. More so, NDSiP may not disperse uniformly throughout the polymer matrix which can create localized regions where the flame retardant is ineffective, reducing the overall protective effect and leading to a decline in FPI. Similarly, the 5 wt% NDP loading increased the FIGRA indicating the potential of unmodified ND to increase fire growth, which can be detrimental to fire safety. This could be attributed to changes in thermal conductivity, combustion characteristics and matrix integrity compared to NDSiP or PA6. The increased thermal conductivity may have led to more rapid heat transfer throughout the material, potentially allowing flames to spread more quickly. However, the various NDSiP weight fractions reduced the FIGRA significantly as shown in Fig. 3f, indicating a potent reduction in fire intensity in case of fire accidents [49].

Furthermore, the FR properties of the composites were assessed using the UL-94 and the LOI standards. The results shown in Table 3 indicate a clear trend in the performance of PA6 composites with varying percentages of NDSiP. As the percentage of NDSiP increases, the LOI values also increase, suggesting improved flame retardancy. For instance, the PA6/NDSiP 5 % sample achieves the highest LOI of 31.2 % and a V-0 rating, which is indicative of excellent flame retardancy properties. The dripping behavior observed in the samples, particularly in PA6 and PA6/NDP, may also influence their practical applications, as materials that drip during combustion can pose additional hazards. The ignition of cotton was noted in pristine PA6 and PA6/NDP samples, indicating their propensity to cause flame spread in case of a fire accident. The data shown in Table 2 demonstrates that the addition of NDSiP to PA6 significantly improves its flame retardancy, as evidenced by the increasing LOI values and improved UL-94 ratings.

3.4. Gas evolution

TG-IR was used to study the evolved gaseous products released during the thermal degradation of PA6 and NDSiP composites and the results are presented in Fig. 4. As may be seen from the 3D TG-IR shown in Fig. 4(a–c), the intensity of the evolved gases decreased for PA6/NDP 5 % and even further for PA6/NDSiP 5 % composites compared to PA6. However, the composites showed early onset simmering gas release due to the high thermal conductivity of the ND resulting in the early decomposition of the organic moieties, which releases con-combustible gases and radicals that dilute the volatile compounds. As shown in the absorbance spectra in Fig. 4(d), extensive release of water molecules is noted around 3700 cm^{-1}–3800 cm^{-1} in the PA6/NDP 5 % and the PA6/NDSiP 5 % composites compared to PA6 due to the heat sink and hydrating effect of thermally conductive ND. Also, peaks corresponding to hydrocarbon fragments such as methane, ethane, and ethene around 3015, ~2970 cm^{-1}, carbonyl compounds around 1713 cm^{-1}, – 1655 cm^{-1} [50], aromatic compounds in the range of 1100 cm^{-1} – 960 cm^{-1} as well as overlapping NH_3 peaks around 965 and 930 cm^{-1}) can be seen in PA6 and the composites. It is instructive to note that, the hydrocarbon fragments, carbonyl compounds, and gaseous related to aromatic compounds are highly suppressed for PA6/NDSiP 5 % composites as shown in Fig. 4(d); indicating the potential effects of the silicone-phosphor modification in minimizing toxic gases effect based on the Lambert Beer's law [51]. The dynamics of the volatile gases released during pyrolysis by PA6 and ND composites are shown by Gram-Schmidt curves in Fig. 4(e). A significant decrease in the intensity of absorption of PA6/NDSiP 5 % composite is observed compared to PA6/NDP 5 % and pristine PA6 indicating the efficiency of the phosphor-silicone modification in reducing toxic pyrolysis products release by PA6. Similarly, Fig. 4(f–i) shows a significant gaseous suppression and delay related hydrocarbons, carbon monoxide, carbon dioxide, carbonyl compounds and aromatic compounds (Fig. S2). This phenomenon could be attributed to the flame-inhibition and suppression interaction by phosphorous radicals, volatile silicone compounds made up of low molecular weight aliphatic siloxanes [52], N_2 and NH_3 gases with volatile groups in PA6. The combination of these reactions resulted in the formation of stable adducts that inhibit the release of gaseous products release. The presence of phosphorous can also induce char formation during degradation whereas the ND and silicone can help stabilize the char further, which further acts as a protective barrier, suppressing volatile emissions.

Table 2
UL-94 and LOI values of pristine PA6 and PA6/ND composites.

Samples	T_1 (s)	T_2 (s)	Dripping	Ign. Cotton	Rating	LOI
PA6	10 ± 2	14 ± 2	Yes	Yes	V-2	23.1
PA6/NDP	8 ± 3	7 ± 2	Yes (Heavy)	Yes	V-2	24.2
PA6/NDSiP 1 %	4 ± 2	2 ± 1	Yes	No	V-0	26.3
PA6/NDSiP 2 %	2 ± 1	2 ± 1	No	No	V-0	27.4
PA6/NDSiP 3 %	2 ± 1	1 ± 1	No	No	V-0	29.2
PA6/NDSiP 5 %	0	0	No	No	V-0	31.2

Note: T_1 and T_2 refer to the duration of burning after the removal of flame sources from the polymer.

3.5. Residue char characterization and FR mechanism

SEM micrographic char analysis is essential for understanding flame retardancy mechanisms, hence the SEM images of PA6/NDP 5 %, PA5/NDSiP 3 %, and PA6/NDSiP 5 % char are shown in Fig. 5(a–c). It can be observed that the PA6/NDP 5 % char showed a more porous and fragile structure due to possible catalytic degradation of the char resulting from the high thermal conductivity of NDP. Upon modification with phosphor-silicone, thus PA6/NDSiP 3 % loading, the char appears comparatively compact and robust, albeit with visible cracks, fissures, and a rugged surface. As the content of NDSiP increases to 5 wt%, the char appeared more compact, and uniform with visibly fewer cracks or fissures observed with the 3 wt% loading. Based on these observations, the Raman spectra of the char were to understand the ratio of graphitic to amorphous char present in the char, and the results are presented in Fig. 5(d–f). From the ID/IG ratios, the char stability increases with the increasing loading of NDSiP in the order PA6/NDSiP 5 % > PA6/NDSiP 3 % > PA6/NDP. The improved char quality could be attributed to the condensed phase mechanism of phosphorous along with the ability of silicone compounds to promote crosslinking within the polymer matrices during thermal degradation, combined with the thermal stability of NDP and the reduced catalytic effect.

Based on the TG-IR results, SEM micrographic, and Raman spectroscopic char analysis, the FR mechanism is proposed and illustrated in Fig. 5g. Upon exposure to heat, the thermally conductive ND catalyzes the early breakdown of the phosphor-silicone compound into low molecular weight siloxane [52] and phosphorus species [53]. The onset degradation of the phosphorus in the condensed creates phosphoric-carbonaceous complexes as well as phosphoric radicals which reduces the overall combustion and enhances radical capturing of volatiles. During this process, PA6 begins to degrade by cessation of the amide linkages (hexylamine, caprolactam) to yield amines, carbon dioxide (CO_2), ethylene, methanol, and other volatile short-chain hydrocarbons and aromatic compounds. During this process, the evolution of phosphorus radicals and siloxane complexes interacts with the volatile hydrocarbons and other combustible products from PA6 degradation and reduces the burning rate while catalyzing the formation of stable phosphoric-siloxane ND char complex in the condensed phase.

To unravel the complex mechanism of char formation of the

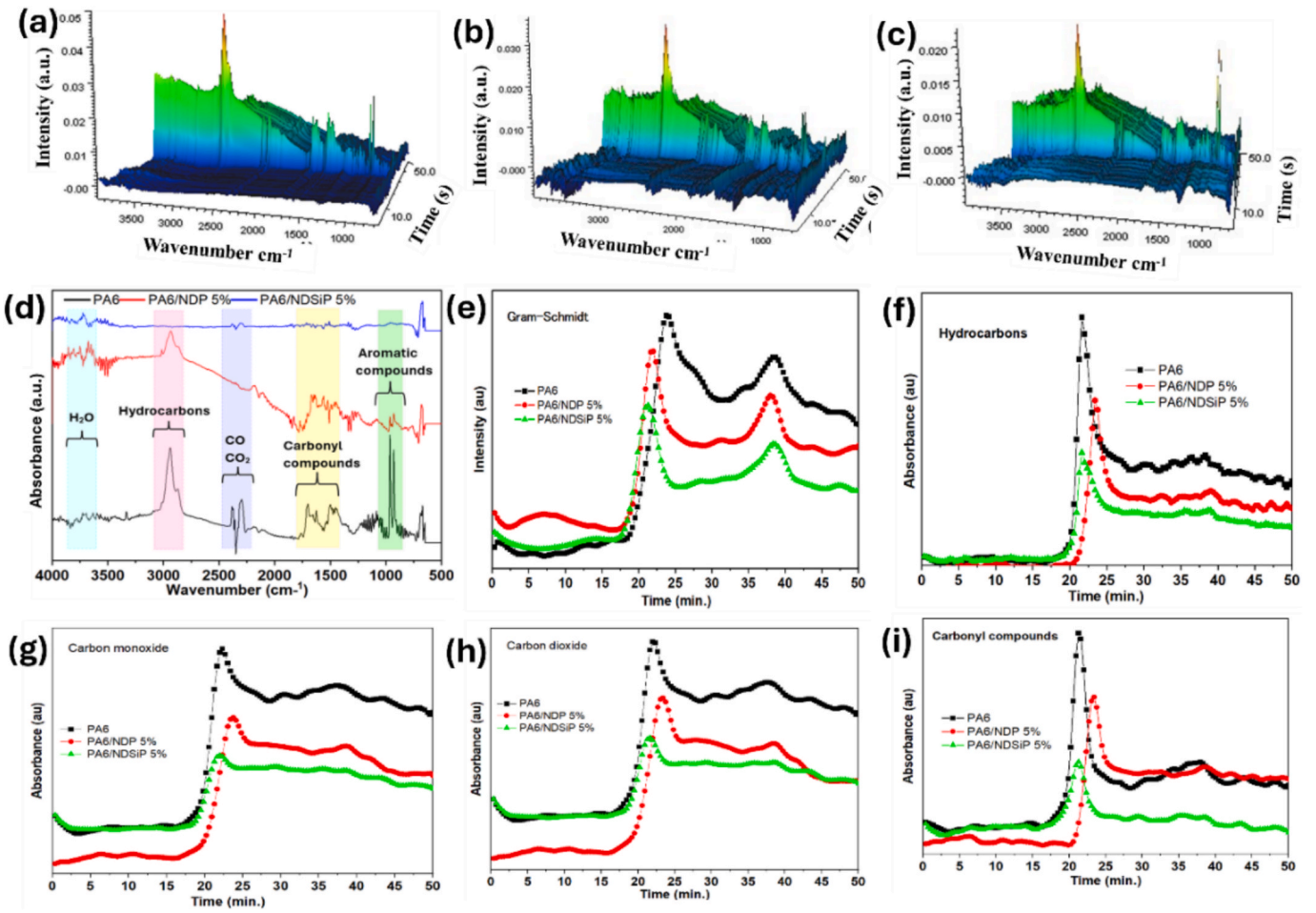

Fig. 4. 3D TG-IR gas evolution of (a) Pristine PA6, (b) PA6/NDP 5 %, (c) PA6/NDSiP 5 %, (d) Absorbance spectra of PA6 and PA6/NDSiP composites, (e) Gram-Schmidt absorption curves of PA6, PA6/NDP and PA6/NDSiP composites, Volatile gases evolution of PA6 and PA6/NDSiP composites (f) Hydrocarbons, (g) carbon monoxide (h) carbon dioxide and (i) carbonyl compounds.

composites, MD-ReaxFF simulation was used to determine the molecular behavior of both PA6 and PA6/NDSiP composites under extreme temperature conditions, providing additional insights into the flame-retardant mechanism of PA6/NDSiP composites beyond the experimental understanding. As shown in Fig. 6(a), when PA6 and PA6/NDSiP were heated at 2500 K after 500 ps, the bonding force between the PA6 monomers was significantly disassociated due to the extreme heat energy. This caused the linear structure of PA6 to break down into minor aliphatic fragments (i.e. C_2H_4, C_3H_6, C_4H_6, etc.), CO, and H_2O similar to the TG-IR results. The PA/NDSiP system also produced similar gases as shown in Fig. 6(c), however, a more compact carbonaceous structure was produced due to the presence of ND, which provided abundant carbon sources as shown in Fig. S3a. The product species evolved during the heating process and their final distribution is shown in Fig. 6(b–d). For PA6, it can be observed that the excessive heat energy induced a rapid evolution of mono-olefin, such as ethylene (C_2H_4) and propylene (C_3H_6). These combustible alkene gases were formed due to the rapid β-scission reaction at the local polymer chains, contributing to the heat release during combustion. The NDSiP, on the other hand, altered the species spectrum with an early disassociation of the SiP component, which significantly increased the number of C_2H_4 due to the local disassociation at the propyl and the alkyl group of the APTES. The NDSiP generally reduced the number of other hydrocarbons, such as C_3H_6, C_4H_6, and CH_4N, however, a notable increase in aromatic hydrocarbon (i.e., C_6H_6) can be observed (See Fig. 6(c–d), indicating an increase in the system's aromaticity. The obvious increase in C_2H_4 in the PA6/NDSiP composite is due to the rapid oxidation of the sp^2-bonded carbons present in ND. To determine the carbon density of the system, the RDF spectrum of the C–C pairs in the heated PA6 and PA6/NDSiP system was studied, and the results are shown in Fig. 6(e). It can be observed that the immense C–C double bonds within the ethylene (C_2H_4) and propylene (C_3H_6) of PA6 had an interatomic carbon distance of 1.35 Å, dominating the distribution. Also, interatomic carbon distances of 1.19 Å can be seen due to the C–C triple bond within the allenes. For PA6/NDSiP, the C–C peaks were significantly shifted toward 1.42 Å, corresponding to the bond distance of the graphitic structure during the charring process [54]. At the same time, the peak at 1.16 Å indicates the presence of a more compact carbonaceous structure compared to PA6. This can be ascribed to several reasons including the presence of ND, which provided more carbonaceous elements to form an aromatic structure (see Fig. S3a), and the ability of phosphorous components to form oxidized phosphoric-carbonaceous clusters in condense-phase as shown by the crystalline P-O-C structure in Fig. S3b. This could also be influenced by the thermal cracking of sp^3 carbons in ND with the increasing decomposition temperature. This crosslinking architecture of the composites primarily results from the phosphorylation and condensation reactions of SiP, which lead to the formation of a crystalline phosphorus oxide structure. This structure is bonded to the polymer chain through P-O-C and P-O-P linkages. The thermally stable char complex disrupts the burning process, resulting in the reduction of organic volatiles and reduces the concentration of oxygen in the flame zone, leading to the eventual suppression of the combustion.

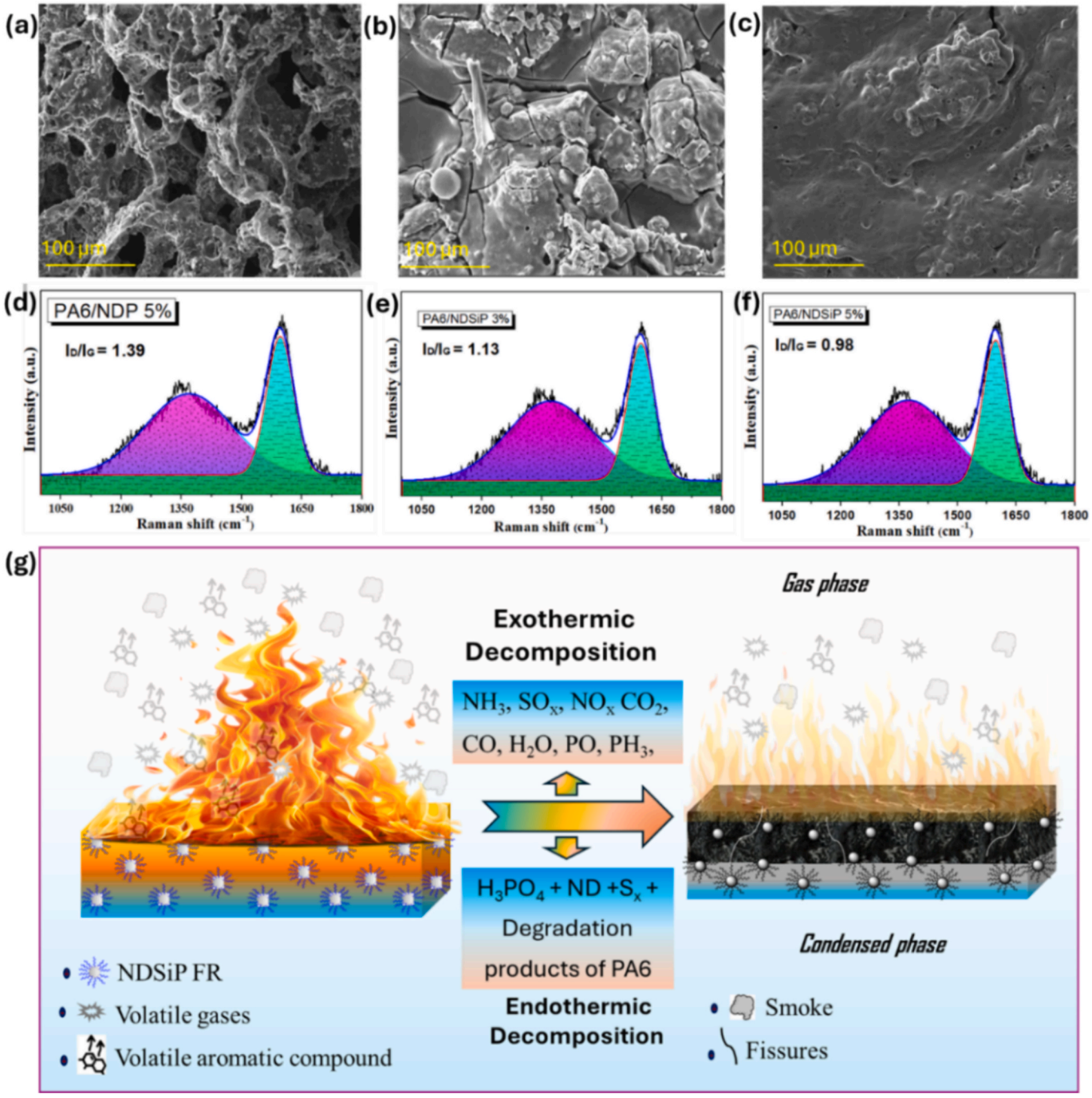

Fig. 5. SEM micrographs of char residue of PA6/ND composites (a) PA6/NDP 5 %, (b) PA6/NDSiP 3 %, (c) PA6/NDSiP 5 %. Raman spectra of residual char, (d) PA6/NDP 5 %, (e) PA6/NDSiP 3 %, (f) PA6/NDSiP 5 %, and (g) Proposed flame retardant mechanism of PA6/NDSiP composites.

3.6. Thermo-pyroelectric response

Ferroelectric composites are essential for a variety of applications because of their improved dielectric properties, improved electromechanical coupling, and adaptability in different sectors [55]. Therefore, the pyroelectric properties of PA6/ND composites were investigated, and the results are shown in Fig. S4, Table 3. PA6 and its composites demonstrated varied ferroelectric responses (i.e., P-E loops) as indicated by the complex interactions of the electric field intensity, material composition and the changes in polarization. As shown in Fig. S4(a), PA6 demonstrated hysteresis behavior characteristic of viscoelastic plastic deformation in response to changes in voltage with a concomitant rise in polarization. Similarly, the PA6/NDP 5 % and PA6/NDSiP 5 % exhibited similar but greater viscoelastic plastic deformation with higher polarization values (Table 3 and Fig. S4(b–c)) as indicated by the size and shape of their P-E loops in response to the changing voltage. At elevated voltages, the P-E loops enlarge, indicating improved ferroelectric response and heightened polarization, which are essential for optimal performance in sensors and actuators [56]. The improved ferroelectric response of PA6/NDP 5 % and PA6/NDSiP 5 % as demonstrated by the increases in remnant polarization, switching polarization, average permittivity, capacitance, and improved resistivity (see Table 3) is due to the presence of the nanofillers. The increased ferroelectric response of PA6/NDP 5 % and PA6/NDSiP 5 % can be attributed to the high surface area of ND, its inherent polarizability, and the presence of functional groups on the surface which possibly

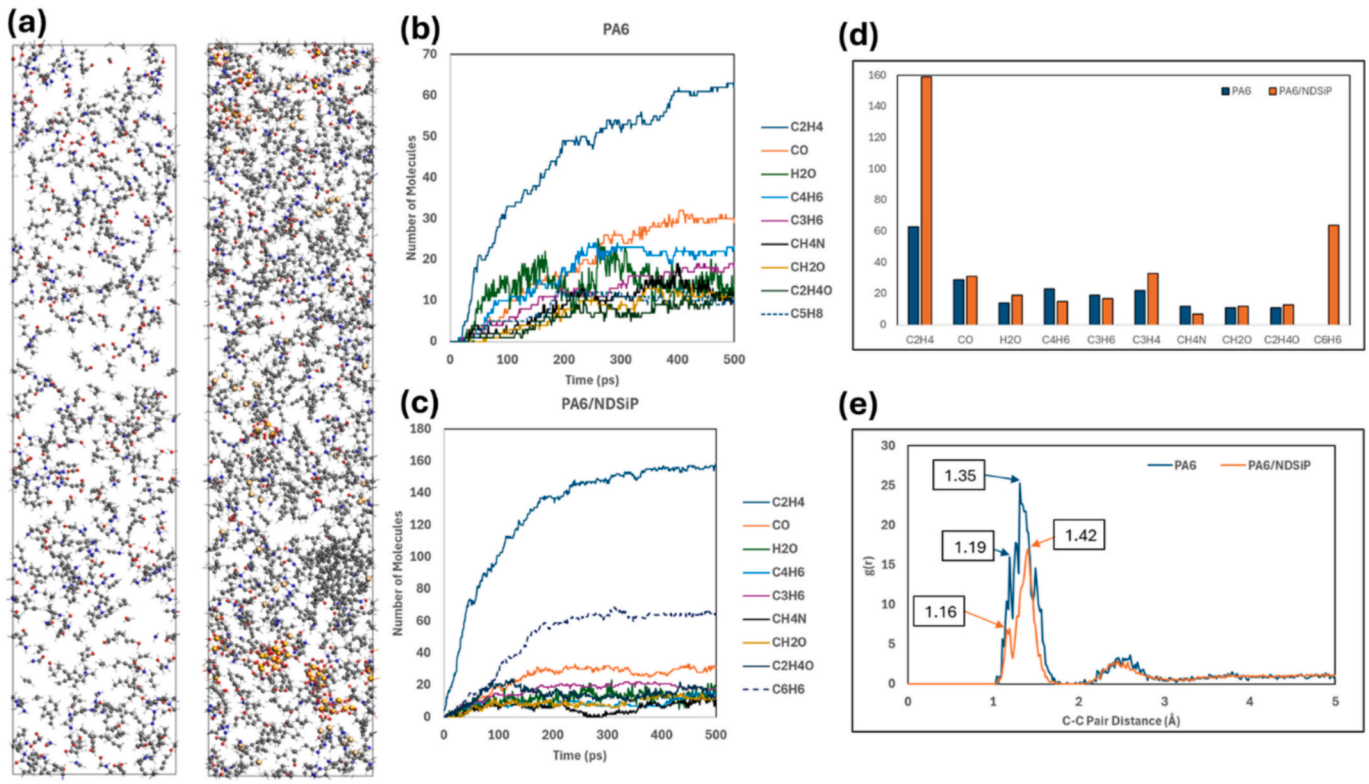

Fig. 6. MD-ReaxFF simulations of PA6 and PA6/NDSiP (a) Snapshots of the systems after heating, (b) Product species distribution of PA6, (c) Product species distribution of PA6/NDSiP, (d) Final number of product species, (e) The RDF Spectrum of C–C pair of PA6 and PA6/NDSiP system.

Table 3
Ferroelectric properties of PA6, and ND composites at room temperature.

Samples	Pmax (μC/cm^2)	$P_{remanant}$ (μC/cm^2)	Psw (μC/cm^2)	dPsw (μC/cm^2)	Average Permittivity	Capacitance (F)	Resistivity (Ω)	Wloss [uJ/cm^2]
PA6	0.205525	0.0265713	2.22E-01	1.95E-01	5.41E + 01	1.60E-11	4.57E + 09	2.33E + 02
PA6/NDP 5 %	1.63155	0.785751	2.17E + 00	9.83E-01	1.10E + 02	1.63E-11	1.50E + 09	3.74E + 03
PA6/NDSiP 3 %	0.446421	0.149427	5.62E-01	3.65E-01	5.60E + 01	1.65E-11	1.64E + 09	2.26E + 04
PA6/NDSiP 5 %	0.580322	0.208752	7.20E-01	5.10E-01	6.60E + 01	1.95E-11	1.37E + 09	2.58E + 04

promoted hydrogen bonding with the amide groups in PA6, further contributing to the increased polarization. These properties combined with the silicone and phosphorus moiety create strong interfacial interactions with the PA6 matrix resulting in localized dipole moments at the interface leading to increases in the overall ferroelectric response.

Fig. 7(d) and (e) depict the thermo-pyroelectric responses of PA6, PA6/NDP 5 % and PA6/NDSiP 5 % at 1500 kV, respectively, demonstrating the materials' reactions to temperature variations. It can be observed that the introduction of nano-filler enhanced the polarization with the increasing temperature compared to the pure PA6. Notably, the PA6/NDP 5 % recorded marginally higher polarization across the entire temperature swoop compared to the PA6/NDSiP 5 % due to differences in interfacial interactions, dielectric properties, temperature stability, and the efficiency of the polarization switching mechanism shown in Table 3 (dPsw (μC/cm^2)). This indicates that certain compositions produce enhanced polarization in response to temperature changes, which is essential for applications necessitating accurate mechanical actuation [57]. The pyroelectric coefficient ($-\partial P/\partial T$) over various temperatures for pristine PA6, PA6/NDP 5 %, and PA6/NDSiP 5 % are illustrated in Fig. 6(e). The increasing $\partial P/\partial T$ with the rising temperature by the composites indicates the impact of temperature on the energy conversion efficiency of the materials. The increasing pyroelectric coefficient with the rising temperature for NDP and NDSiP could be attributed to their improved thermal conductivity and the presence of sp^3 hybridized carbon atoms in ND contributing to a strong dipole moment. For NDSiP, the interaction between silicone and ND led to improved charge separation and mobility due to the additional surface defects, which contributed to localized dipoles resulting in the enhanced pyroelectric response. The phenomenon suggests that the composites enhanced charge generation and possess improved sensitivity to temperature changes and potentially more favorable phase transitions compared to pristine PA6, making it more suitable for applications requiring efficient thermal-to-electrical energy conversion. The energy loss profile of PA6 and its nanocomposites depicted in Fig. 7(f), demonstrate the influence of temperature on energy dissipation (heat). It can be observed that PA6/NDP 5 % dissipates relatively higher energy with the increase in temperature suggesting its suitability for thermal management which is crucial for enhancing the performance of electronic materials [58]. The comparative analysis of the composites indicates that piezoelectric performance is affected by the interaction of electric field strength, temperature, and material composition. Understanding these aspects of PA6 composites is essential for optimizing

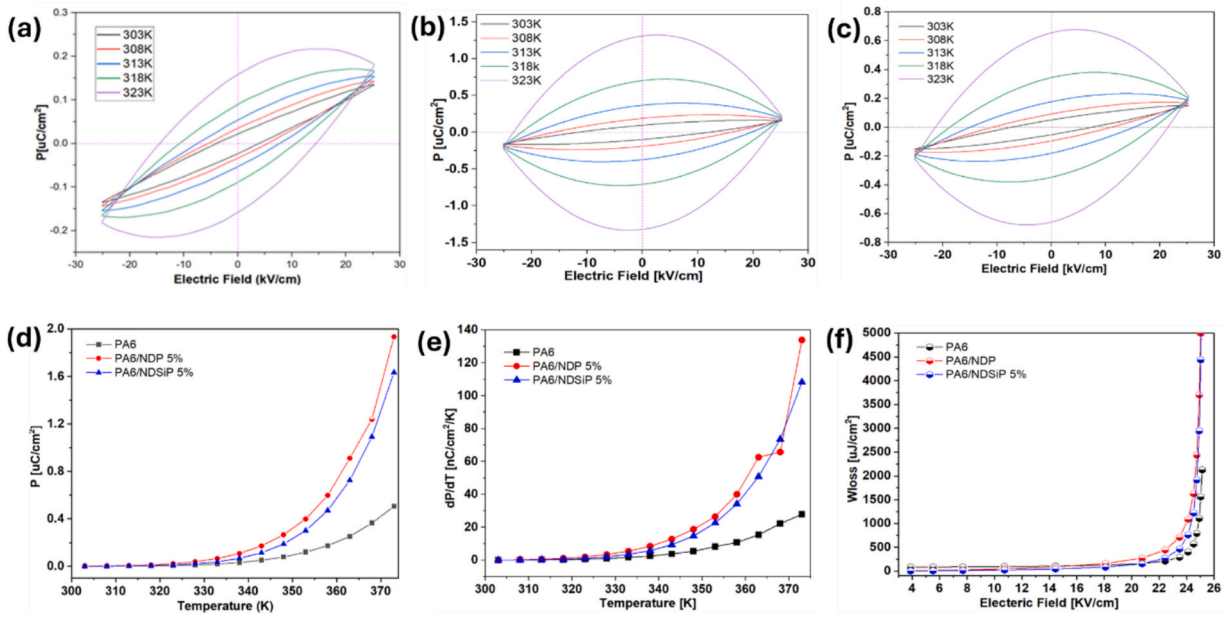

Fig. 7. Thermopyroelectric response of PA6 and composites 1500 kV (d) PA6, (e) PA6/NDP 5 % (f) PA6/NDSiP 5 %. (g) Effect of temperature on polarization at 1500 kV) (h) Pyroelectric coefficient ($-\partial P/\partial T$) at different temperatures, (i) Energy loss curve of PA6 and composites.

materials fabrication for energy harvesting and sensor applications.

3.7. Thermal management

Based on the energy loss profile from the P-E loop, the thermal management properties of the composites were investigated and the

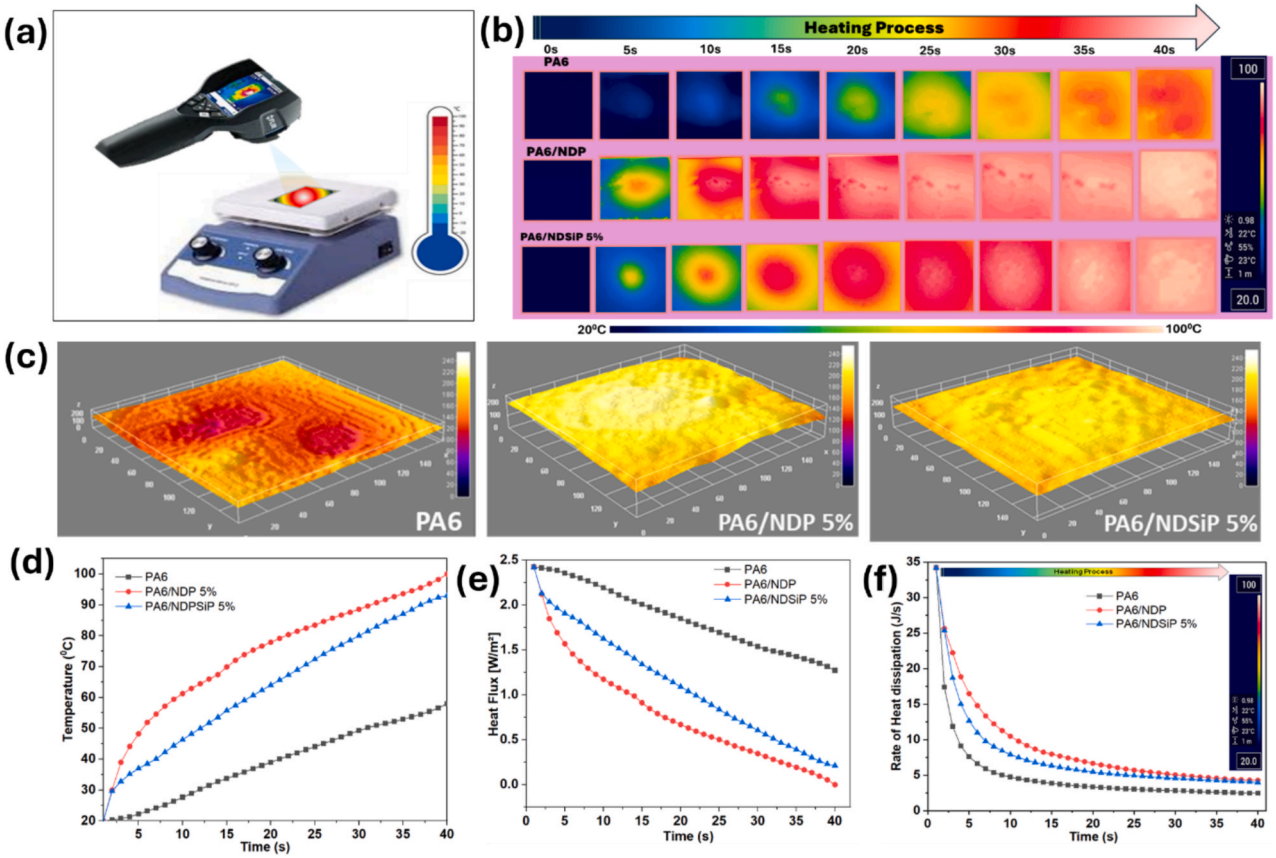

Fig. 8. Thermal management of properties of PA6/ND composites (a) Experimental set-up for thermal management evaluation of composite films, (b) thermal IFR images of samples at different times (c) 3D tomographic maps of PA6 and PA6/NDP 5% and PA6/NDSiP 5% composites, (d) Change in temperature over time, (e) Rate of heat flux over time and (f) rate of heat dissipation through PA6 and PA6/ND composites over time.

results are shown in Fig. 8. As shown in the thermal IFR image in Fig. 8 (a,b), the rate of heat dissipation through pristine PA6 is slower compared to PA6/NDP 5 % and PA6/NDSiP 5 % indicating the potential of overheating of electronic components made with pristine PA6. Compared with PA6/NDP 5 % composite, the rate of heat dissipation through polymer is faster and higher due to the high thermal conductivity of pristine ND. However, after surface modification of ND (NDSiP), the rate of heat dissipation decreased slightly compared to the unmodified ND as shown in Fig. 8b. The relative slow heat dissipation rate of NDSiP compared to pristine ND is due to the presence of the organosilicon and phosphorus molecules which created additional interfaces and boundaries on the ND surface, leading to increased

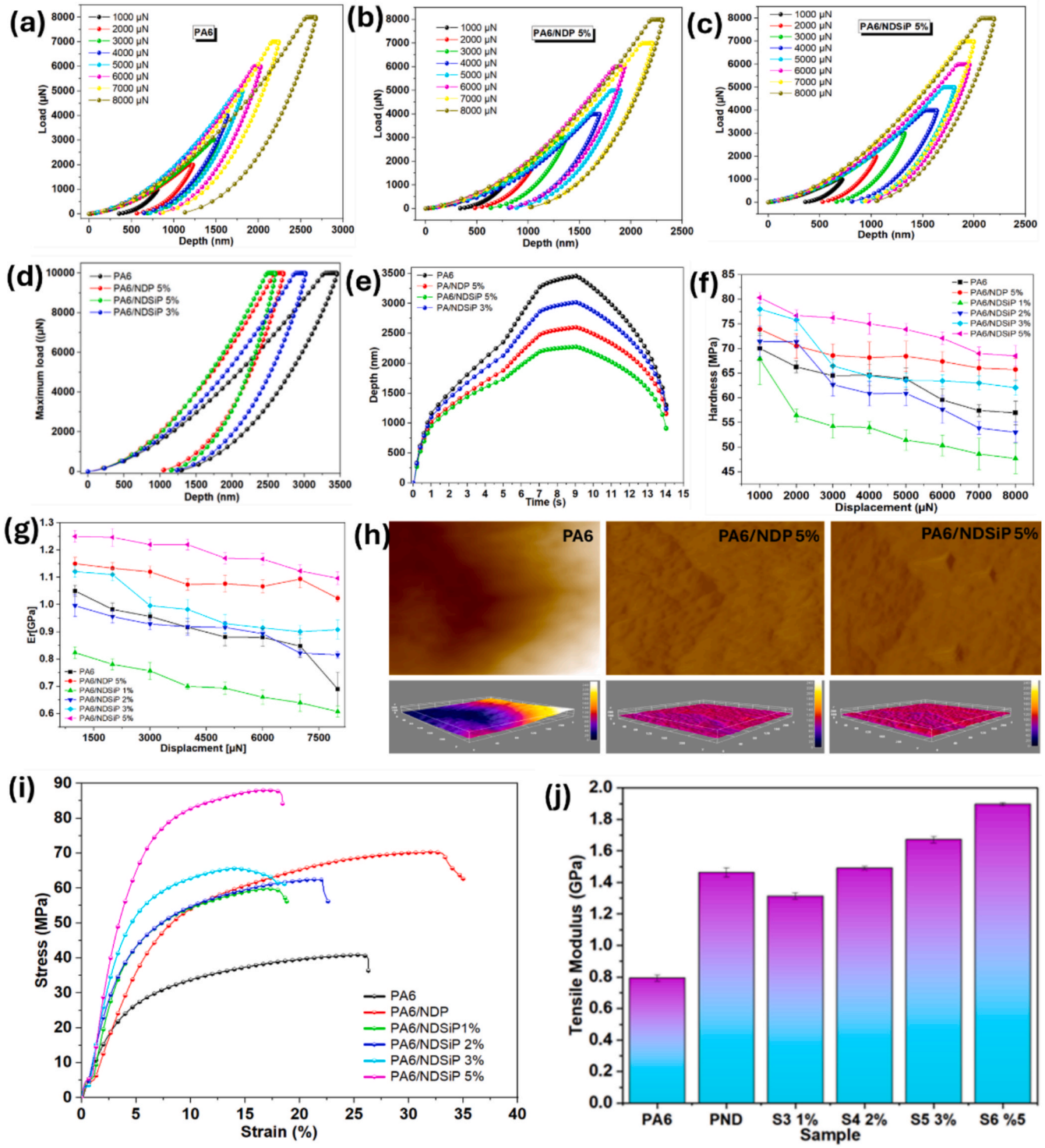

Fig. 9. Load vs displacement curves of PA6 and PA6/ND composites (a) PA6, (b) PA6/NDP 5 % (c) PA6/NDSiP 5 %, (d) Comparative PA6 and PA6/ND composites at maximum load of 10,000 µN, (e) A plot of indentation depth against time for PA6 and PA6/ND composites, (f) Hardness of PA6 and PA6/ND composites, (g) Indentation modulus of PA6 and PA6/ND composites, (h) Indentation depths and corresponding 3D maps of PA6 and PA6/ND composites. Bulk material mechanical properties of PA6 and PA6/ND composites (i) Tensile strength vs elongation at break and (j) True tensile modulus. Note: *S1- PA6, S2 – PA/NDP, S3 – PA6/NDSiP 1 %, S4 – PA6/NDSiP 2 %, S5 – PA6/NDSiP 3 %, S6 – PA6/NDSiP 5 %.*

scattering of phonons and reduced thermal conductivity as noted in Fig. 2(d). Heat dissipative polymer composites offer versatile and effective solutions for heat control in electronic applications, combining lightweight with excellent thermal and mechanical properties. The 3D thermographic map of the samples was taken after 40 s, and as shown in Fig. 8(c), the PA6 composite shows a concentration of heat within the composite compared to PA6/NDSiP 5 % and PA6/NDP composite, thus confirming the poor heat dissipative properties of pristine PA6. Furthermore, it can be observed that the surface temperature of PA6/NDP 5 % was constantly higher than the PA6/NDSiP 5 % and PA6 composites due to the faster phonon heat transfer mechanism of ND (see Fig. 7(d)). Based on these results, the heat flux was determined according to Eq. (4) based on Fourier's law [59]:

$$q = K\frac{dT}{dx} \tag{4}$$

where q is the heat flux, K is the thermal conductivity of the composite and $\frac{dT}{dx}$ is the temperature gradient. The heat flux curve reveals a trade-off between initial performance and sustained capability. PA6 showed a higher rate of heat flux, limiting its heat dissipative ability where immediate heat management is required. PA6/NDP 5 %, however, showed a similar initial trend but the heat flux declined portentiously over time due to the higher rate of heat dissipation. PA6/NDSiP 5 %, on the other hand, provides a more stable and sustainable option for effective heat dissipation, making it a better choice for applications requiring thermal stability and long-term thermal management. This trend is critical for selecting materials based on the specific thermal demands, especially for electronic systems a good balance between thermal management and flame retardancy is important. Similarly, as shown in Fig. 8(f), the rate of heat dissipation for PA6/NDP 5 % appears marginally higher than PA6/NDSiP 5 % and PA6 in the entire 40 s – consistent with the trend observed in Fig. 8(b). The overall poor heat dissipative ability of PA6 over time in contrast to the composites shows its potential to provide better long-term thermal management due to the lower thermal resistance resulting from the enhanced phonon heat transport properties of NDs [60].

3.8. Nanomechanical properties

Understanding the nanomechanical and bulk material properties of polymer composites is essential for designing materials for electronics, automotive, and aerospace applications. As shown in Fig. 9. the nanoscale deformation of the polymer composites is exemplified by the load–displacement curves. It can be observed that in Fig. 9(a–c), the load–displacement curves for pure PA6 at different loads exhibited a nonlinear relationship similar to the composites – PA6/NDP 5 % and PA6/NDSiP 5 %. Under varying loads from 1000 μN to 8000 μN, the pristine polymer and its composites displayed a similar characteristic of elastic deformation as well as plastic deformation, however, the penetration depth varied from one composite to another. As shown in Fig. 9 (a–c) the maximum indentation depth for PA6 at a maximum load of 8000 μN, reached 2.5 μm whereas the PA6/NDP 5 % and PA6/NDSiP 5 % reached 2.4 μm and 2.3 μm respectively, indicating less creased plastic deformation and an improvement in hardness and modulus. Subsequently, as the maximum load of 10,000 μN was applied on PA6 and the composites, the maximum penetration depth of the composites PA6/NDP 5 %, PA6/NDSiP 3 %, and PA6/NDSiP 5 % dropped to ~45 % compared to the pristine PA6 as shown in Fig. 8(d–e). The decreased indentation of the composites could be attributed to the enhanced interfacial adhesion between the polymer chains and the filler, which hinders the easy mobility of the polymer chains. More importantly, the NDSiP composite showed improved hardness with higher nanofiller loading as shown by the diminishing penetration depth due to the improved interfacial bonding between the polymer chains and the phosphor-silicone particles, leading to a more cohesive material structure.

To further evaluate the plastic deformation hardness and the elastic modulus of PA6 and its composites, the half-space elastic deformation theory was used according to the Oliver-Pharr method [61]. Sneddon's elastic contact model [62] was used to calculate the elastic modulus from the indentation experiments according to Eq. (5).

$$E_{r=}\frac{s\sqrt{\pi}}{2\beta\sqrt{A_c}} \tag{5}$$

where, S represents the unloading stiffness, defined as the initial slope of the unloading and displacement curve at the maximum displacement. Ac denotes the predictable contact area between the tip and the substrate, while β is the constant (β = 1.167) specific to the typical Berkovich tip utilized for this measurement. Similarly, the contact hardness was determined using Eq. (6) based on the maximum load and the square of the contact depth.

$$H = \frac{P_{max}}{A_c} \tag{6}$$

where H represents the contact hardness, with P_{max} being the maximum load applied and A_c as the contact area of the Berkovich indenter (A_c=24.5*h_c^2). The load–displacement curves depicting the maximum applied force to the contact depth for all samples are illustrated in Fig. 9 (f and g). It can be observed from Fig. 9(g) that PA6/NDSiP 5 % hardness increased significantly with the increasing load compared to PA6. However, the 5 wt% of NDP loading demonstrates near uniform hardness and modulus throughout the increasing load range due to the extremely stiff and high surface area of nanodiamonds, which allows for effective load distribution across the composite matrix, minimizing localized deformation. Higher displacement enhances the indenter-filler particle effective contact area, improving load transfer. However, at NDSiP composite containing 3 wt% filler loading, the hardness increased at low load and decreased at higher loading. When the NDSiP content increased to 5 wt%, the hardness improved significantly across the entire displacement range (see Fig. 9(f) due to improved interfacial bonding and the alter the possible damping characteristics of silicons, allowing it to absorb energy better during deformation resulting in uniform distribution of stress and less localized deformation, contributing to the improved hardness. Similarly, the computed modulus followed almost the same hardness trend as shown in Fig. 9(g) due to the improved load distribution over the filler resulting from the improved interfacial adhesion. To verify the extent of depth, the nano-indentation marks and their corresponding 3D tomographs for pure PA6 and their nanocomposites were taken during the loading and unloading cycle at maximum load (10000 μN), and the results are shown in Fig. 9(h). It can be observed that PA6 had the deepest depth as indicated by the AFM image and the 3D tomographic map, followed by PA6/NDP 5 % and PA6/NDSiP 5 %, showing only a few scratches at three different spots.

The bulk material tensile properties were evaluated by measuring the stress–strain curves and Young's modulus of the PA6 and its nanocomposites to clarify the tensile dynamics for real-world applications. As shown in Fig. 9(i), the tensile strength of the composites (PA6/NDSiP with 1 %, 2 %, 3 %, 4 %, and 5 %) showed an increasing trend until it reached a maximum value of 89 Mpa compared to 40 MPa by PA6, representing approximately ~123 % increase, however, the elongation at break reduced by ~43 %. Similarly, the 5 wt% NDSiP loading enhanced the Young Modulus by ~138 %. The improved tensile strength and modulus could be attributed to the inherent exceptional hardness and strength of nanodiamonds [63] and the interfacial bonding between the PA6 matrix by the silicon moieties [64]. The combined effect of nanodiamonds and silica enhanced the absorption capacity of the composite, allowing it to better dissipate energy during the tensile loading, resulting in increased load-bearing capacity.

4. Conclusions

In this study, a novel phosphor-silicon decorated nanodiamond (NDSiP) was successfully synthesized and incorporated into polyamide 6 (PA6) composites to enhance their multifunctional properties. NDSiP was melt-blended with PA6 at varying weight fractions, and its structural, thermal, flame-retardant, and mechanical properties were systematically evaluated. The structural characteristics of NDSiP were confirmed through X-ray diffraction (XRD), Fourier-transform infrared spectroscopy (FTIR), Raman spectroscopy, transmission electron microscopy (TEM), and scanning electron microscopy-energy dispersive X-ray spectroscopy (SEM-EDX). The thermal conductivity of PA6/NDP (5 %) composites exhibited a 424 % increase compared to pristine PA6. However, following modification with SiP, the thermal conductivity increased gradually, with 5 wt% NDSiP loading achieving an overall enhancement of 302 %. The thermal stability of the composites showed a slight reduction with increasing NDSiP loading, attributed to the early degradation onset of the surface-modifying functional groups. The flame-retardant properties of the composites demonstrated significant improvements, with notable reductions in peak heat release rate (PHRR), total heat release (THR), average effective heat combustion (AEHC), flame retardancy index (FRI), and specific heat release rate (SHRR) by 40.7 %, 45.3 %, 28.1 %, 160 %, and 286.4 %, respectively. A V-0 rating was attained in the limiting oxygen index (LOI) test, with an LOI value of 31.2 %. Additionally, TG-IR results revealed a significant decrease in volatile gases, hydrocarbons, and aromatic products, further confirming the material's flame resistance. Molecular dynamics (MD)-ReaxFF simulations indicated that the flame-retardant mechanism was predominantly active in the condensed phase, facilitated by a shift in C–C peaks towards a graphitic orientation at 1.42 Å and 1.16 Å. This effect was further supported by the presence of ND and the phosphorylation/condensation reactions of SiP. In terms of heat dissipation, NDP (5 %) composites dissipated heat more efficiently than both PA6/NDSiP (5 %) and pristine PA6, owing to the enhanced phonon heat transport of pristine ND, consistent with the energy loss profile observed in ferroelectric tests. However, the PA6/NDSiP (5 %) composite provided better long-term thermal management, attributed to its superior flame-retardant properties. The maximum polarization of the composites increased to 1.615 μC/cm2 for PA6/NDP (5 %) and 0.5803 μC/cm2 for PA6/NDSiP (5 %), compared to 0.2056 μC/cm2 in pristine PA6. The pyroelectric coefficient of PA6/NDP (5 %) and PA6/NDSiP (5 %) exhibited a gradual increase from ~330 K to 375 K, driven by phase transitions, enhanced domain dynamics, increased polarization, and dielectric property modifications in PA6. Similarly, the average capacitance increased from 16.0 pF (pristine PA6) to 16.3 pF (PA6/NDP 5 %) and 19.5 pF (PA6/NDSiP 5 %). Additionally, significant improvements were observed in nanoindentation hardness and modulus, with bulk material tensile stress and modulus increasing by 123 % and 138 %, respectively.

Declaration of Generative AI and AI-assisted technologies in the writing process

The authors declare that no AI assistive technologies were used during the preparation of the manuscript.

CRediT authorship contribution statement

Benjamin Tawiah: Writing – review & editing, Writing – original draft, Methodology, Investigation, Formal analysis, Data curation, Conceptualization. **Sana Ullah:** Writing – original draft, Software, Investigation, Formal analysis, Data curation. **Ivan Miguel De Cachinho Cordeiro:** Writing – review & editing, Writing – original draft, Software, Methodology, Investigation, Formal analysis, Data curation. **Anthony C.Y. Yuen:** Writing – review & editing, Validation, Software, Methodology, Investigation, Formal analysis, Conceptualization. **Yang Ming:** Writing – review & editing, Validation, Investigation, Formal analysis, Data curation. **Mohammad Z. Rahman:** Writing – review & editing, Writing – original draft, Investigation, Formal analysis, Data curation. **Daming Chen:** Writing – review & editing, Software, Formal analysis, Data curation. **Wei Cai:** Writing – review & editing, Validation, Software, Methodology, Formal analysis, Data curation. **Zheng Guangping:** Writing – review & editing, Validation, Supervision, Project administration, Formal analysis. **Bekeshev Amirbek:** Writing – review & editing, Validation, Supervision, Project administration, Formal analysis. **Lyazzat Tastanova:** Writing – review & editing, Validation, Investigation, Formal analysis. **Bin Fei:** Writing – review & editing, Validation, Supervision, Resources, Funding acquisition, Formal analysis, Conceptualization.

Funding

This research was supported by the Hong Kong Polytechnic University projects (1-WZ2H, 1-BBCB, 1-CD8E), and the Innovation and Technology Council of the Hong Kong SAR (Project number ITP/023/22TP).

Declaration of competing interest

The authors declare that they have no known competing financial interests or personal relationships that could have appeared to influence the work reported in this paper.

Acknowledgement

The authors acknowledge the technical efforts of Dr. M. Adnan (KUST, Pakistan) for this manuscript.

Appendix A. Supplementary material

Supplementary data to this article can be found online at https://doi.org/10.1016/j.cej.2025.162249.

Data availability

Data will be made available on request.

References

[1] S. Simões, *High-performance advanced composites in multifunctional material design: state of the art, challenges, and future directions*, Materials 17 (23) (2024) 5997.
[2] X.-S. Yi, X. An, *Developments of high-performance composites by innovative ex situ concept for aerospace application*, J. Thermoplast. Compos. Mater. 22 (1) (2009) 29–49.
[3] S.B. Shen, H. Ishida, *Development and characterization of high-performance polybenzoxazine composites*, Polym. Compos. 17 (5) (1996) 710–719.
[4] J. Yang, et al., *High-performance composite phase change materials for energy conversion based on macroscopically three-dimensional structural materials*, Mater. Horiz. 6 (2) (2019) 250–273.
[5] J. Liu, et al., *Enhancing fire safety, electromagnetic interference shielding, and photothermal conversion performances of wearable polyamide fabrics through eco-friendly coatings*, Sustain. Mater. Technol. 40 (2024) e00949.
[6] Q. Li, Q. Wang, *Ferroelectric polymers and their energy-related applications*, Macromol. Chem. Phys. 217 (11) (2016) 1228–1244.
[7] Z. Liu, et al., *Strong synergistic effects between boron-containing compounds and aluminum diethylphosphinate for enhanced fire safety and mechanical properties of polyamide 6*, ACS Appl. Polym. Mater. (2024).
[8] B. Huang, et al., *A strategy toward improving flame retardancy and thermal oxidative stability of polyamide 6 based on cuprous diethylphosphinate*, Polymer 302 (2024) 127046.
[9] M.B. Mahmud, et al., *Developing highly flame-retardant PA6-based composites via in-situ PPS nanofiber network*, Polymer (2024) 127296.
[10] B. Tawiah, et al., *Flame retardant poly (lactic acid) biocomposites reinforced by recycled wool fibers-thermal and mechanical properties*, Express Polym. Lett. 13 (8) (2019) 697–712.
[11] M. Sabet, *Advancements in halogen-free polymers: exploring flame retardancy, mechanical properties, sustainability, and applications*, Polym.-Plast. Technol. Mater. (2024) 1–25.

[12] S. Fu, et al., *Some basic aspects of polymer nanocomposites: a critical review*, Nano Mater. Sci. 1 (1) (2019) 2–30.
[13] Y. Luo, et al., *Advances in nanomaterials as exceptional fillers to reinforce carbon fiber-reinforced polymers composites and their emerging applications*, Polym. Compos. 46 (1) (2025) 54–80.
[14] H.-S. Jung, K.C. Neuman, *Surface modification of fluorescent nanodiamonds for biological applications*, Nanomaterials 11 (1) (2021) 153.
[15] I.P. Chang, et al., *Facile surface functionalization of nanodiamonds*, Langmuir 26 (5) (2010) 3685–3689.
[16] G. Reina, et al., *Chemical functionalization of nanodiamonds: opportunities and challenges ahead*, Angew. Chem. Int. Ed. 58 (50) (2019) 17918–17929.
[17] B. Nan, Y. Zhan, C.-A. Xu, *A review on the thermal conductivity properties of polymer/nanodiamond nanocomposites*, Polym.-Plast. Technol. Mater. 62 (4) (2023) 486–509.
[18] C. Shuai, et al., *Surface modification of nanodiamond: toward the dispersion of reinforced phase in poly-l-lactic acid scaffolds*, Int. J. Biol. Macromol. 126 (2019) 1116–1124.
[19] A. Krueger, D. Lang, *Functionality is key: recent progress in the surface modification of nanodiamond*, Adv. Funct. Mater. 22 (5) (2012) 890–906.
[20] S. Angela, et al., *Surface modification of nanodiamonds*, Nanodiamonds Anal. Biol. Sci. Princ. Appl. (2023) 52–72.
[21] C. Presti, et al., *Surface functionalization of detonation nanodiamonds by phosphonic dichloride derivatives*, Langmuir 30 (30) (2014) 9239–9245.
[22] L. Li, et al., *Improving thermal conductivity of poly(vinyl alcohol) composites by using functionalized nanodiamond*, Compos. Commun. 23 (2021) 100596.
[23] Ü. Tayfun, M. Doğan, *Flame-retardant properties of fullerene and nanodiamond-based polymer nanocomposites*, in: *Flame Retardant Nanocomposites*, Elsevier, 2024, pp. 263–286.
[24] A. Kausar, *Nanodiamond reinforcement effects in thermosetting matrices—design, functional features and significance*, J. Macromol. Sci. A 61 (10) (2024) 724–741.
[25] Y. Zhang, et al., *A critical review of nanodiamond based nanocomposites: synthesis, properties and applications*, Compos. B Eng. 143 (2018) 19–27.
[26] Galli, G., *Structure, stability and electronic properties of nanodiamonds.* Computer-Based Modeling of Novel Carbon Systems and Their Properties: Beyond Nanotubes, 2010: p. 37-56.
[27] B. Zeng, et al., *Improved pyroelectric performances of functionally graded graphene nanoplatelet reinforced polyvinylidene fluoride composites: experiment and modelling*, Compos. A Appl. Sci. Manuf. 176 (2024) 107883.
[28] Z. Wang, J. Liu, B. Chu, *Schiff base organic molecular crystals/ferroelectric polymer composite for photo-pyroelectric conversion*, J. Mater. Chem. C 12 (21) (2024) 7807–7814.
[29] S. Pattipaka, et al., *Ceramic-based dielectric materials for energy storage capacitor applications*, Materials 17 (10) (2024) 2277.
[30] R.F. Gibson, *A review of recent research on mechanics of multifunctional composite materials and structures*, Compos. Struct. 92 (12) (2010) 2793–2810.
[31] B. Chaudhary, et al., *Multifunctional composite structures with embedded conductive yarns for shock load monitoring and failure detection*, Smart Mater. Struct. 33 (3) (2024) 037001.
[32] A. Ciampaglia, et al., *Multifunctional material design for strain sensing: carbon black effect on mechanical and electrical properties of polyamides*, Compos. Struct. 304 (2023) 116373.
[33] S. Baloda, H. Kumar, *Tailoring thermal and mechanical properties: friction stir techniques for hybrid composites*, in: Utilizing friction stir techniques for composite hybridization, IGI Global, 2024, pp. 135–158.
[34] P. Sagar, S. Sangwan, *Characterization methods for assessing hybrid nanomaterial performance*. Technological applications of nano-hybrid composites, IGI Global, 2024.
[35] Y. Wu, et al., *Highly aligned graphene aerogels for multifunctional composites*, Nano-Micro Lett. 16 (1) (2024) 118.
[36] H. Ruan, et al., *Fluorinated interface engineering targeting high-performance multifunctional composites of BN/aramid nanofibers*, Compos. A Appl. Sci. Manuf. 178 (2024) 107975.
[37] M. Shao, et al., *Multifunctional composites with a polymer matrix containing carbon nanotubes: a study of structural, physicochemical and operational characteristics*, Fullerenes, Nanotubes, Carbon Nanostruct. 33 (1) (2025) 66–76.
[38] A. Kausar, *Technical competence of nanodiamond nanocomposites in energy sector (solar cells, fuel cells, batteries, supercapacitors)-state-of-the-art*, Adv. Energy Conver. Mater. (2025) 57–82.
[39] R.G. Ryan, et al., *Impact of surface functionalization on the quantum coherence of nitrogen-vacancy centers in nanodiamonds*, ACS Appl. Mater. Interf. 10 (15) (2018) 13143–13149.
[40] A. Krueger, *The chemistry of nanodiamond* (2014).
[41] X. Wang, et al., *Consecutive deposition of amorphous SiO_2 interlayer and diamond film on graphite by chemical vapor deposition*, Carbon 117 (2017) 126–136.
[42] S. Turner, et al., *Determination of size, morphology, and nitrogen impurity location in treated detonation nanodiamond by transmission electron microscopy*, Adv. Funct. Mater. 19 (13) (2009) 2116–2124.
[43] T. Tegafaw, et al., *Production, surface modification, physicochemical properties, biocompatibility, and bioimaging applications of nanodiamonds*, RSC Adv. 13 (46) (2023) 32381–32397.
[44] V. Mochalin, et al., *The properties and applications of nanodiamonds*, Nano-Enabled Med. Appl. (2020) 313–350.
[45] V. Efremov, et al., *Thermal stability of detonation-produced micro and nanodiamonds*, IOP Publishing, 2018.
[46] Q. Wang, et al., *Sp2@ sp3 effect of a nanodiamond greenly driving epoxy with superior fire safety and mechanical properties*, ACS Sustain. Chem. Eng. 11 (48) (2023) 16902–16913.
[47] N. Zhao, et al., *Nanodiamond coating in energy and engineering fields: synthesis methods, characteristics, and applications*, Small (2024) 2401292.
[48] B. Tawiah, et al., *Simultaneous fire safety enhancement and mechanical reinforcement of poly(lactic acid) biocomposites with hexaphenyl (nitrilotris(ethane-2,1-diyl))tris (phosphoramidate)*, J. Hazard. Mater. 380 (2019) 120856.
[49] B. Tawiah, et al., *Microporous boron based intumescent macrocycle flame retardant for poly(lactic acid) with excellent UV protection*, Chem. Eng. J. 402 (2020) 126209.
[50] Y. Lu, et al., *Strong synergistic effects between P/N-containing supramolecular microplates and aluminum diethylphosphinate for fire-retardant PA6*, Compos. A Appl. Sci. Manuf. 176 (2024) 107834.
[51] T.G. Mayerhöfer, S. Pahlow, J. Popp, *The bouguer-beer-lambert law: shining light on the obscure*, Chem. Phys. Chem. 21 (18) (2020) 2029–2046.
[52] A. Soroceanu, et al., *The thermal behavior of silicone-based composite materials and the assessment of the gases that result from the thermal degradation process*, Mater. Sci. Eng. B 312 (2025) 117855.
[53] Y. Luo, et al., *Preparation and performance of waterborne polyurethane coatings based on the intumescent flame retardant of boron, phosphorus, and nitrogen*, J. Appl. Polym. Sci. 142 (7) (2025) e56481.
[54] I.D.C. Cordeiro, et al., *Characterising flame-retardant mechanism of phosphorous-containing intumescent coating on polyethylene via ReaxFF MD simulations*, Chem. Eng. J. 480 (2024) 148169.
[55] S. Ullah, et al., *Highly enhanced electrothermal properties of 001-textured Pb-free ferroelectric (Ba, Ca)(Ti, Zr, Sn) O_3 for energy harvesting and solid-state cooling*, J. Eur. Ceram. Soc. 45 (1) (2025) 116830.
[56] L. Jin, F. Li, S. Zhang, *Decoding the fingerprint of ferroelectric loops: comprehension of the material properties and structures*, J. Am. Ceram. Soc. 97 (1) (2014) 1–27.
[57] M. Enyan, et al., *Advances in smart materials soft actuators on mechanisms, fabrication, materials, and multifaceted applications: a review*, J. Thermoplast. Compos. Mater. (2024), 08927057241248028.
[58] G. Sebald, E. Lefeuvre, D. Guyomar, *Pyroelectric energy conversion: optimization principles*, IEEE Trans. Ultrason. Ferroelectr. Freq. Control 55 (3) (2008) 538–551.
[59] T. Kawaguchi, et al., *Fourier's law of heat transfer and its implication to cell motility*, Biosystems 81 (1) (2005) 19–24.
[60] A. Bain, et al., *Thermal Conductance of Nanoparticles: A Study of Phonon Transport in Functionalized Nanodiamond Suspensions*, American Society of Mechanical Engineers, 2020.
[61] G. Pharr, W. Oliver, *Measurement of thin film mechanical properties using nanoindentation*, MRS Bull. 17 (7) (1992) 28–33.
[62] I.N. Sneddon, *Boussinesq's problem for a rigid cone*, Math. Proc. Camb. Philos. Soc. 44 (4) (1948) 492–507.
[63] S.M. Fouda, et al., *Flexural properties, impact strength, and hardness of nanodiamond-modified PMMA denture base resin*, Int. J. Biomater. 2022 (1) (2022) 6583084.
[64] Y. Guo, et al., *Effect of silane treatment on adhesion of adhesive-bonded carbon fiber reinforced nylon 6 composite*, Int. J. Adhes. Adhes. 91 (2019) 102–115.